The Astrophysical Journal Supplement Series, 270:5 (30pp), 2024 January https://doi.org/10.3847/1538-4365/ad0787

Stellar Neutrino Emission across the Mass–Metallicity Plane

Ebraheem Farag[1], F. X. Timmes[1], Morgan T. Chidester[1], Samalka Anandagoda[2], and Dieter H. Hartmann[2]
[1] School of Earth and Space Exploration, Arizona State University, Tempe, AZ 85287, USA; ekfarag@asu.edu
[2] Department of Physics and Astronomy, Clemson University, Kinard Lab of Physics, Clemson, SC 29634-0978, USA

Received 2023 September 11; revised 2023 October 16; accepted 2023 October 19; published 2023 December 19

Abstract

We explore neutrino emission from nonrotating, single-star models across six initial metallicities and 70 initial masses from the zero-age main sequence to the final fate. Overall, across the mass spectrum, we find metal-poor stellar models tend to have denser, hotter, and more massive cores with lower envelope opacities, larger surface luminosities, and larger effective temperatures than their metal-rich counterparts. Across the mass–metallicity plane we identify the sequence (initial CNO $\rightarrow$ ^{14}N $\rightarrow$ ^{22}Ne $\rightarrow$ ^{25}Mg $\rightarrow$ ^{26}Al $\rightarrow$ ^{26}Mg $\rightarrow$ ^{30}P $\rightarrow$ ^{30}Si) as making primary contributions to the neutrino luminosity at different phases of evolution. For the low-mass models we find neutrino emission from the nitrogen flash and thermal pulse phases of evolution depend strongly on the initial metallicity. For the high-mass models, neutrino emission at He-core ignition and He-shell burning depends strongly on the initial metallicity. Antineutrino emission during C, Ne, and O burning shows a strong metallicity dependence with ^{22}Ne$(\alpha, n)^{25}$Mg providing much of the neutron excess available for inverse-β decays. We integrate the stellar tracks over an initial mass function and time to investigate the neutrino emission from a simple stellar population. We find average neutrino emission from simple stellar populations to be 0.5–1.2 MeV electron neutrinos. Lower metallicity stellar populations produce slightly larger neutrino luminosities and average β decay energies. This study can provide targets for neutrino detectors from individual stars and stellar populations. We provide convenient fitting formulae and open access to the photon and neutrino tracks for more sophisticated population synthesis models.

Unified Astronomy Thesaurus concepts: Neutrino astronomy (1100); Nuclear astrophysics (1129); Stellar physics (1621); Stellar evolutionary tracks (1600); High energy astrophysics (739)

1. Introduction

The next core-collapse (CC) supernova in the Milky Way or one of its satellite galaxies will be an opportunity to observe the explosion of a massive star across the electromagnetic, gravitational, and particle spectra. For example, neutrinos with energies $\lesssim$10 MeV have played a prominent role in stellar physics (Alekseev et al. 1987; Bionta et al. 1987; Hirata et al. 1987, 1988; Bahcall 1989; Borexino Collaboration et al. 2014, 2018, 2020) and particle physics (Bahcall 1989; Ahmad et al. 2002; Ackermann et al. 2022). Maps of $\geqslant$1 TeV neutrinos from the Galactic plane are consistent with a diffuse emission model of neutrinos whose analysis includes the supernova remnant and pulsar wind nebula outcome(s) of CC events (IceCube Collaboration 2023).

Ongoing technological improvements in detector masses, energy resolution, and background abatement will allow the global SuperNova Early Warning System network (Al Kharusi et al. 2021) to observe new signals from different stages of the life cycle of individual stars or the aggregate signal from a stellar population with multikiloton detectors such as Super-Kamiokande (Simpson et al. 2019; Harada et al. 2023), SNO+ (Allega et al. 2023), KamLAND (Abe et al. 2023), Daya Bay (An et al. 2023), DUNE (Acciarri et al. 2016), JUNO (Yang & JUNO Collaboration 2022) and the upcoming HyperKamiokande (Abe et al. 2016).

Ongoing stellar neutrino searches aim to detect pre-supernova neutrinos, which allow new tests of stellar and neutrino physics (e.g., Brocato et al. 1998; Odrzywolek et al. 2004; Kutschera et al. 2009; Odrzywolek 2009; Patton et al. 2017a, 2017b; Kato et al. 2017, 2020a; Yusof et al. 2021; Kosmas et al. 2022) and enable an early alert of an impending CC supernova to the electromagnetic and gravitational-wave communities (Beacom & Vogel 1999; Vogel & Beacom 1999; Mukhopadhyay et al. 2020; Al Kharusi et al. 2021). They also aim to explore the diffuse supernova neutrino background (Bisnovatyi-Kogan & Seidov 1984; Krauss et al. 1984; Hartmann & Woosley 1997; Ando & Sato 2004; Porciani et al. 2004; Horiuchi et al. 2009; Beacom 2010; Anandagoda et al. 2020; Suliga 2022; Anandagoda et al. 2023) and neutrinos from the helium-core nitrogen flash (Serenelli & Fukugita 2005), compact object mergers (Kyutoku & Kashiyama 2018; Lin & Lunardini 2020), tidal disruptions of stars (Lunardini & Winter 2017; Reusch et al. 2022; Winter & Lunardini 2023), and pulsational pair-instability supernovae (Leung et al. 2020).

Farag et al. (2020) introduced the idea of a neutrino Hertzsprung–Russell diagram (νHRD) with a sparse grid of models. Each model started from the zero-age main sequence (ZAMS) and ended at a final fate but only at solar metallicity. They found all masses produce a roughly constant neutrino luminosity L_ν during core H burning on the main sequence (MS), and confirmed that low-mass ($M_{\rm ZAMS} < 8\ M_\odot$) red giant branch (RGB) models with $M_{\rm ZAMS} \leqslant\ 2\ M_\odot$ undergo large increases in L_ν during the helium flash (nitrogen flash for neutrinos; Serenelli & Fukugita 2005) and subsequent subflashes. They also found that He burning in asymptotic giant branch (AGB) models produces sharp increases in L_ν from thermal pulses (TPs), and significantly larger L_ν from the hotter and denser cores of later evolutionary stages culminating at the onset of CC in high-mass ($M_{\mathrm{ZAMS}} \geqslant 8\,M_{\odot}$), nonrotating, single-star models. A photon Hertzsprung–Russell diagram (γHRD) provides information about the stellar surface, while a νHRD can serve as a diagnostic tool of the stellar interior.

Changes in the initial metallicity Z of a model changes the structure of the model through the equation of state (EOS; Saumon et al. 1995; Timmes & Swesty 2000; Rogers & Nayfonov 2002; Irwin 2004; Potekhin & Chabrier 2010; Jermyn et al. 2021; Bauer 2023), radiative opacity (Iglesias & Rogers 1993, 1996; Ferguson et al. 2005; Ferguson & Dotter 2008; Poutanen 2017), conductive opacity (Cassisi et al. 2007; Blouin et al. 2020), nuclear energy generation rate (Angulo et al. 1999; Cyburt et al. 2010; Sallaska et al. 2013; deBoer et al. 2017; Farag et al. 2022), gravitational sedimentation (Bauer et al. 2020), and mass loss by line-driven winds (Sanyal et al. 2017; VandenBerg et al. 2022).

The coupling between these pieces of stellar physics and neutrino production from thermal (Itoh et al. 1996a) and weak reaction processes (Fuller et al. 1985; Oda et al. 1994; Langanke & Martínez-Pinedo 2000; Nabi et al. 2021) suggests that changes in Z can cause changes in a νHRD, and upon integration, the neutrino emission from a simple stellar population model.

This article is novel in exploring stellar neutrino emission across the mass–metallicity plane. This study can provide targets for neutrino detectors from individual stars and stellar populations. Section 2 describes the mass–metallicity grid and stellar physics, Section 3 presents overall features and drivers across the mass–metallicity plane, Section 4 analyzes low-mass tracks, Section 5 details high-mass tracks, Section 6 explores neutrino emission from a simple stellar population model, and Section 7 summarizes our results.

Important symbols are defined in Table 1. Acronyms and terminology are defined in Table 2.

2. Mass–Metallicity Plane and Stellar Physics

We model the evolution of single, nonrotating stars over a wide range of initial masses and metallicities, from the pre-main sequence (PMS) to the final fate. Figure 1 shows the mass–metallicity plane for 70 M_{ZAMS} models distributed in the range $0.2\,M_{\odot} \leqslant M_{\mathrm{ZAMS}} \leqslant 150\,M_{\odot}$ for six initial metallicities $\log(Z/Z_{\odot}) = 0.5, 0, -0.5, -1, -2, -3$, where we choose $Z_{\odot} = 0.0142$ (Asplund et al. 2009). This mass–metallicity plane spans the range of single stars found in the Galaxy (Edvardsson et al. 1993; Almeida-Fernandes et al. 2023; Ratcliffe et al. 2023), and aids estimates of the neutrino emission from simple stellar population models.

We use `MESA` version r15140 to construct our stellar models (Paxton et al. 2011, 2013, 2015, 2018, 2019; Jermyn et al. 2023). We follow MIST (Choi et al. 2016) to scale the H mass fraction X, He mass fraction Y, and metallicity Z

$$Y = Y_{\mathrm{p}} + \left(\frac{Y_{\odot} - Y_{\mathrm{p}}}{Z_{\odot}}\right) Z \tag{1}$$

$$X = 1 - Y - Z, \tag{2}$$

where we adopt the primordial He abundance $Y_{\mathrm{p}} = 0.249$ (Planck Collaboration et al. 2016), $Y_{\odot} = 0.2703$, and $Z_{\odot} = 0.0142$ with mass fractions from Asplund et al. (2009).

Table 1
Important Symbols

Name	Description	Appears
A	Atomic number	2
D	Element diffusion coefficient	2
E	Energy	3.2
ϵ	Average neutrino energy	5.1
g	Gravitational acceleration	3.2
H	Pressure scale height	3.2
κ	Opacity	3.2
k_{B}	Boltzmann constant	3.2
L	Luminosity	1
M	Stellar mass	1
μ	Mean molecular weight	2
n	Number density	2
η	Neutron excess	2
R	Stellar radius	4.2
ρ	Mass density	3.2
P	Pressure	3.2
T	Temperature	2
τ	Time or timescale	4.2
X	Mass fraction	2
X	Hydrogen mass fraction	2
Y	Abundance	2
Y	Helium mass fraction	2
Y_e	Electron fraction	2
Z	Metal mass fraction	1
Z	Atomic charge	2

Note. Some symbols may be further subscripted, for example, by c (indicating a central quantity), by γ (indicating a photon quantity), or by ν (indicating a neutrino quantity).

Table 2
Acronyms and Terminology

Acronym	Description	Appears
AGB	Asymptotic giant branch	1
CC	Core collapse	1
CHeB	Core helium burning	3
CHeD	Core helium depletion	3
CO	Carbon–oxygen	3.1
EOS	Equation of state	1
γHRD	Photon Hertzsprung–Russell diagram	1
νHRD	Neutrino Hertzsprung–Russell diagram	1
HB	Horizontal branch	4
IMF	Initial mass function	6
MLT	Mixing-length theory	2
PMS	Pre-main sequence	2
RGB	Red giant branch	1
RSG	Red supergiant	5
TAMS	Terminal-age main sequence	3.1
TP	Thermal pulse	1
WD	White dwarf	2
ZAMS	Zero-age main sequence	1
Low-mass	$M_{\mathrm{ZAMS}} < 8\,M_{\odot}$	1
High-mass	$M_{\mathrm{ZAMS}} \geqslant 8\,M_{\odot}$	1

For the low-mass models, we chose the Reimers wind mass-loss scheme (Reimers 1977) with an efficiency of 0.5 on the RGB, and Blöckers wind mass-loss scheme (Blöcker 2001) with an efficiency of 1.0 on the AGB. All low-mass models terminate as a white dwarf (WD) at $L = 10^{-3}\,L_{\odot}$, even if the evolution is longer than the age of the Universe.

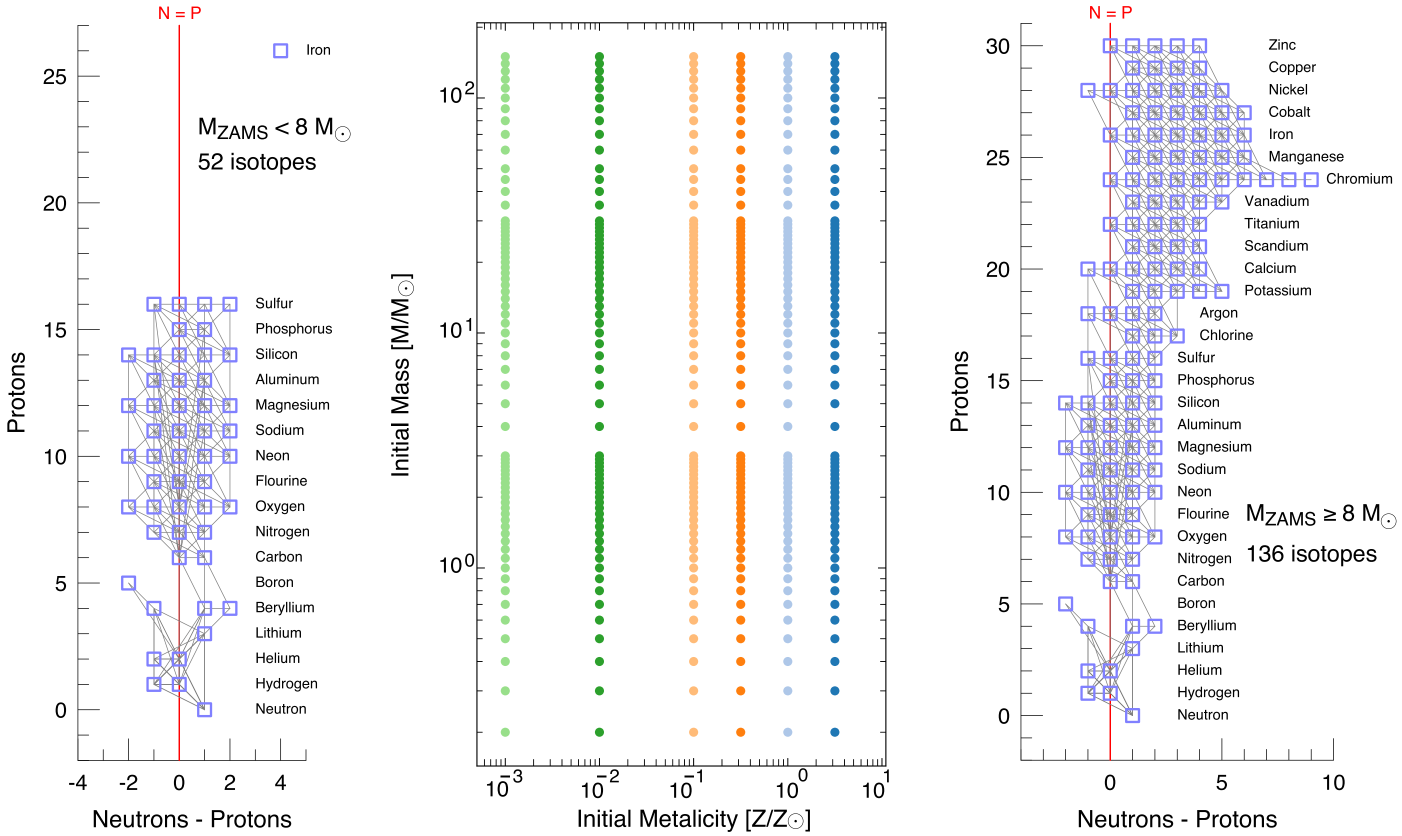

Figure 1. Coverage in the mass–metallicity plane (center). The *x*-axis is the initial *Z* of a model relative to solar, and the *y*-axis is $M_{\rm ZAMS}$ of a model relative to solar. Six metallicities, each marked with a different color, and 70 masses at each metallicity (circles) span the mass–metallicity plane. The nuclear reaction network for low-mass (left) and high-mass (right) models is illustrated. These x-axes are the difference in the number of neutrons and protons in an isotope. Positive values indicate neutron-rich isotopes, the zero value is marked by the red vertical line, and negative values indicate proton-rich isotopes. These *y*-axes are the number of protons in an isotope, labeled by their chemical element names. Isotopes in the reaction network are shown by purple squares. Reactions between isotopes are shown by gray lines. Note Fe in the low-mass reaction network does not react with other isotopes. Fe is included for a more consistent specification of the initial composition, hence any microphysics that depends upon the composition including the opacity, equation of state, element diffusion, and neutrino emission.

For the high-mass models, we choose the "Dutch" wind-loss scheme (Nieuwenhuijzen & de Jager 1990; Nugis & Lamers 2000; Vink et al. 2001; Glebbeek et al. 2009) with an efficiency of 1.0 to generate stripped models. All models use an Eddington-gray iterated atmosphere as an outer boundary condition. We apply an extra pressure to the surface (see Section 6.1 of Jermyn et al. 2023) of our AGB and high-mass models to maintain stability of the surface layer in super Eddington regimes where the surface of the model can otherwise run away. The termination age for all high-mass models is at the onset of CC when the infall velocity of the Fe core reaches $100\,{\rm km\,s^{-1}}$. A subset of our models halted prematurely: at core C depletion ($M_{\rm ZAMS} = 8$–$10\,M_\odot$), a stalled Ne/O flame in a degenerate core ($M_{\rm ZAMS} = 11$–$14\,M_\odot$), the onset of pair-instability (C ignition with $M_{\rm He} \gtrsim 45\,M_\odot$), or due to numerical difficulties near the onset of CC.

We adopt a minimum chemical diffusive mixing coefficient of $D_{\rm min} = 10^{-2}\ {\rm cm^2\ s^{-1}}$ from C ignition to the onset of CC to aid the convergence properties of our high-mass models (Farag et al. 2022). To reduce the numerical cost we use operator splitting to decouple the hydrodynamics from the nuclear burning for temperatures above $T = 1 \times 10^9$ K (Jermyn et al. 2023).

We also adopt $\alpha = 1.5$ for the convective mixing-length parameter, and $f_{\rm ov} = 0.016$ and $f_{0,\rm ov} = 0.008$ for the convective overshooting parameters in all convective regions (Herwig 2000; Choi et al. 2016). All stellar models use the MLT++ treatment for superadiabatic convection in the envelopes (Sabhahit et al. 2021). We also damp the velocities in the envelopes of our low-mass AGB models and high-mass models during the advanced burning stages to inhibit the growth of radial pulsations.

Figure 1 illustrates the 52 isotope nuclear reaction network used for low-mass stars and the 136 isotope reaction network used for high-mass models. Extended networks are required to accurately capture the nuclear energy generation, composition and stellar structure profiles, and the neutrino luminosity and spectra from β-processes (Farmer et al. 2016; Patton et al. 2017a, 2017b; Kato et al. 2020a). The 136 isotope network is reliable up to the onset of Si-shell burning, $T \lesssim 4 \times 10^9$ K. At higher temperatures, the paucity of Fe-group isotopes in this reaction network cannot fully capture the nuclear burning (Farmer et al. 2016; Patton et al. 2017a).

Nuclear reaction rates are a combination of NACRE (Angulo et al. 1999) and JINA REACLIB (Cyburt et al. 2010). We use the median $^{12}{\rm C}(\alpha,\gamma)^{16}{\rm O}$ reaction rate from the experimental probability distribution function provided by deBoer et al. (2017), updated in Mehta et al. (2022), and publicly released in Chidester et al. (2022). Reaction rate screening corrections are from Chugunov et al. (2007), which includes a physical parameterization for the intermediate screening regime and reduces to the weak (Dewitt et al. 1973; Graboske et al. 1973) and strong (Alastuey & Jancovici 1978; Itoh et al. 1979) screening limits at small and large values of the plasma-coupling parameter. Weak reaction rates are based, in order of precedence, on Oda et al. (1994), Langanke & Martínez-Pinedo (2000), and Fuller et al. (1985).

Baryon number is conserved in nuclear reactions. Define the abundance of species Y_i by

$$\mathrm{Y}_i = \frac{n_i}{n_B} \tag{3}$$

where n_i is the number density of isotope i and n_B is baryon number density. The number of baryons in isotope i divided by the total number of baryons of all isotopes is the baryon fraction (mass fraction)

$$\mathrm{X}_i = \frac{n_i\, A_i}{n_B} = \mathrm{Y}_i\, A_i, \tag{4}$$

where A_i is the atomic mass number, the number of baryons in an isotope. The mean atomic number is

$$\bar{A} = \frac{\sum n_i A_i}{\sum n_i} = \frac{n_B}{\sum n_i} = \frac{\sum \mathrm{Y}_i A_i}{\sum \mathrm{Y}_i} = \frac{1}{\sum \mathrm{Y}_i}, \tag{5}$$

the mean charge is

$$\bar{\mathrm{Z}} = \frac{\sum n_i \mathrm{Z}_i}{\sum n_i} = \frac{\sum \mathrm{Y}_i \mathrm{Z}_i}{\sum \mathrm{Y}_i} = \bar{A} \sum \mathrm{Y}_i \mathrm{Z}_i, \tag{6}$$

and the electron to baryon ratio (electron fraction) is

$$Y_e = \frac{n_e}{n_B} = \frac{\sum n_i \mathrm{Z}_i}{n_B} = \sum Y_i \mathrm{Z}_i = \frac{\bar{\mathrm{Z}}}{\bar{A}}, \tag{7}$$

where n_e is the free electron number density and the second equality assumes full ionization. The related neutron excess is

$$\eta = \sum (N_i - Z_i)\, Y_i = 1 - 2Y_e, \tag{8}$$

the mean ion molecular weight is

$$\mu_{\mathrm{ion}} = \bar{A}\,, \tag{9}$$

the mean electron molecular weight is

$$\mu_{\mathrm{ele}} = \frac{1}{Y_e} = \frac{\bar{A}}{\bar{\mathrm{Z}}}, \tag{10}$$

and the mean molecular weight is

$$\mu = \left[\frac{1}{\mu_{\mathrm{ion}}} + \frac{1}{\mu_{\mathrm{ele}}}\right]^{-1} = \frac{\bar{A}}{\bar{\mathrm{Z}} + 1} = \frac{n_B}{\sum n_i + n_e}. \tag{11}$$

Across the mass–metallicity plane the dominant thermal neutrino processes in our models are plasmon decay ($\gamma_{\mathrm{plasmon}} \rightarrow \nu + \bar{\nu}$), which scales with the composition as Y_e^3, photoneutrino production ($e^- + \gamma \rightarrow e^- + \nu + \bar{\nu}$), which scales as Y_e, and pair annihilation ($e^- + e^+ \rightarrow \nu + \bar{\nu}$), which also scales as Y_e. All else being equal, as material becomes more neutron rich the neutrino emission from these three dominant processes decreases.

Bremsstrahlung ($e^- +^A Z \rightarrow e^- +^A Z + \nu + \bar{\nu}$), which scales with the composition as $Y_e \bar{\mathrm{Z}}$, and recombination ($e^-_{\mathrm{continuum}} \rightarrow e^-_{\mathrm{bound}} + \nu + \bar{\nu}$) , which scales as $\bar{Z}^{14}/\bar{A}$, play smaller roles. Neutrino emission from these five processes are discussed in Itoh et al. (1989, 1992, 1996a, 1996b) and Kantor & Gusakov (2007) and are implemented, with partial first derivatives, in the `MESA` module `neu`. Differential thermal neutrino emission rates are discussed in Ratković et al. (2003), Dutta et al. (2004), Misiaszek et al. (2006), Odrzywołek (2007), Kato et al. (2015), Patton et al. (2017a), and Dzhioev et al. (2023).

Each of the 420 stellar models in the mass–metallicity grid use 2000–3500 mass zones (lower values occur at ZAMS where there are no composition gradients), with ≃3000 mass zones over the evolution being typical. Each low-mass model uses 1×10^5–3×10^5 time steps depending on the number of thermal pulses (TPs), and each high-mass model uses 2×10^4–5×10^4 time steps. Each model executes on a 16 core node with 2 GHz AMD Epyc 7713 CPUs, with low-mass models consuming 14–21 days and high-mass models using 10–21 days. The uncompressed total data set size is ≃730 GB.

The `MESA` files to reproduce our models, and open access to the photon and neutrino tracks, are available at 10.5281/zenodo.8327401.

3. Overall Mass–Metallicity Features

Here, we present features and drivers of the neutrino emission, first at one metallicity in Section 3.1 and then for all six metallicities in Section 3.2.

3.1. One Metallicity

Figure 2 shows the photon and neutrino light curves for all 70 calculated masses at $Z = 1\,Z_{\odot}$. Both plots begin at the ZAMS, defined when the luminosity from nuclear reactions L_{nuc} is 99% of the total luminosity L, marking a transition from evolution on a thermal timescale to a nuclear timescale.

MS evolution is characterized by stable core H burning, where neutrinos are produced by weak reactions in the proton–proton (pp) chains $\mathrm{p(p,\, e^+}\nu_e)^2\mathrm{H}$, $\mathrm{p(e^-p,}\ \nu_e)^2\mathrm{H}$, $^3\mathrm{He(p,\, e^+}\nu_e)^4\mathrm{He}$, $^7\mathrm{Be(e^-,}\ \nu_e)^7\mathrm{Li}$, and $^8\mathrm{B(e^+}\nu_e)^8\mathrm{Be}$, and the CNO cycles $^{13}\mathrm{N(e^+}\nu_e)^{13}\mathrm{C}$, $^{13}\mathrm{N(e^-,}\ \nu_e)^{13}\mathrm{C}$, $^{15}\mathrm{O(e^+}\nu_e)^{15}\mathrm{N}$, $^{15}\mathrm{O(e^-,}\ \nu_e)^{15}\mathrm{N}$, $^{17}\mathrm{F(e^+}\nu_e)^{17}\mathrm{O}$, $^{17}\mathrm{F(e^-,}\ \nu_e)^{17}\mathrm{O}$, and $^{18}\mathrm{F(e^+}\nu_e)^{18}\mathrm{O}$, where electron capture reactions on CNO nuclei are included (Stonehill et al. 2004).

Models with $M_{\mathrm{ZAMS}} \lesssim 1.2\ M_{\odot}$ have a central temperature $T_{\mathrm{c}} \lesssim 18 \times 10^7$ K and burn H in their cores primarily through the pp chains, with a small fraction from the CNO cycles. For example, based on observations of solar neutrinos, CNO burning accounts for around 1.6% of the current energy generation of the Sun (Naumov 2011; Borexino Collaboration et al. 2020). Models with $M_{\mathrm{ZAMS}} \gtrsim 1.2\ M_{\odot}$ have $T_{\mathrm{c}} \gtrsim 18 \times 10^7$ K and maintain their stability primarily from the CNO cycles (Wiescher et al. 2010). Metal-poor models can produce their own carbon to begin CNO cycle H burning (Mitalas 1985; Wiescher et al. 1989; Weiss et al. 2000; Tompkins et al. 2020). In addition, most of a model's initial Z comes from the CNO and ^{56}Fe nuclei inherited from its ambient interstellar medium. The slowest step in the CNO cycle is proton capture onto ^{14}N, resulting in all the CNO catalysts accumulating into ^{14}N during core H burning.

All light curves in Figure 2 proceed to the terminal-age main sequence (TAMS), defined by core H depletion ($X_{\mathrm{c}} \leqslant 10^{-6}$). The He-rich core contracts as a H-burning shell forms. The higher temperatures of shell H burning can activate the Ne–Na, and Mg–Al cycles (Salpeter 1955; Marion & Fowler 1957; Arnould et al. 1999; José et al. 1999; Izzard et al. 2007; Boeltzig et al. 2022). The light curves then bifurcate depending on M_{ZAMS}.

During He burning the accumulated ^{14}N is converted into the neutron-rich isotope ^{22}Ne through the reaction sequence $^{14}\mathrm{N}(\alpha,\gamma)^{18}\mathrm{F}(,e^+\nu_e)^{18}\mathrm{O}(\alpha,\gamma)^{22}\mathrm{Ne}$, also shown in Figure 2. This sequence is the source of neutrinos powering L_ν through all phases of He burning (Serenelli & Fukugita 2005; Farag et al. 2020).

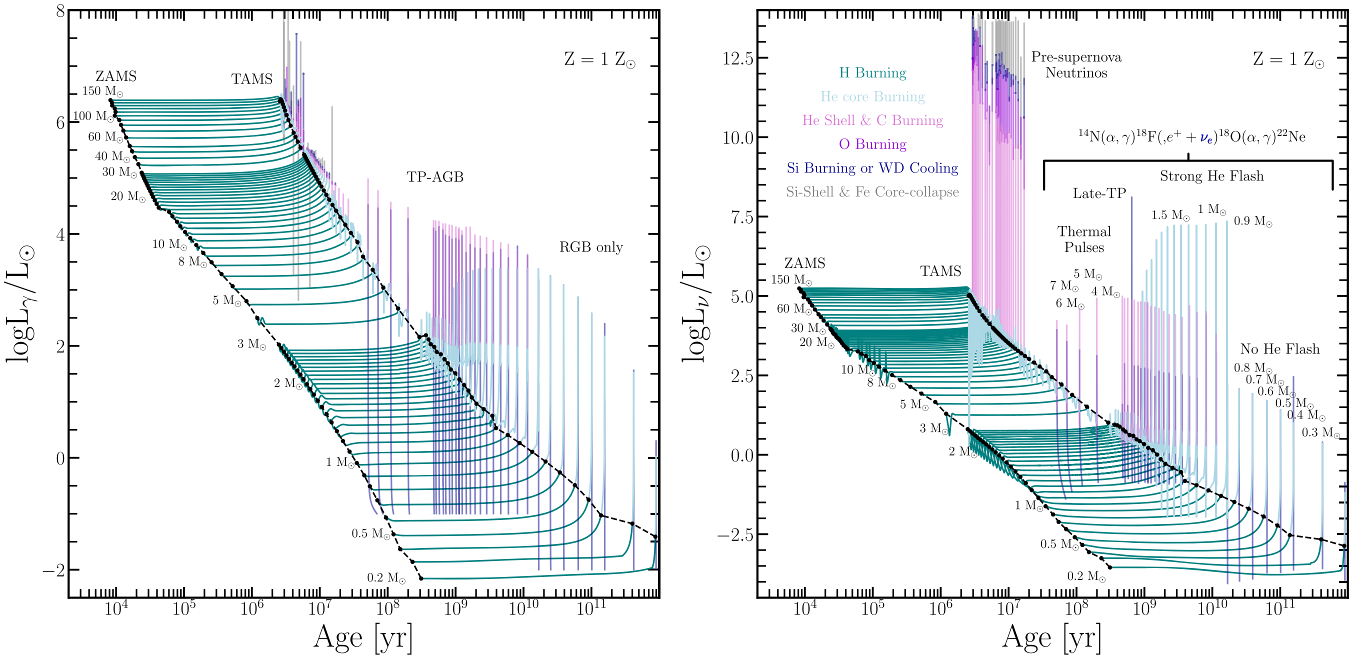

Figure 2. Light curves for photons (left) and neutrinos (right). Tracks span 0.2–150 $M_\odot$ for $Z = 1\ Z_\odot$ and are labeled. Key phases of evolution including the ZAMS (black circles), TAMS (black circles), core He flashes (light green), thermal pulses, and pre-supernova stage are also labeled. The PMS light curves are suppressed for visual clarity. L_ν during the nitrogen flash (He flash for photons) and thermal pulses for the $M < 8\ M_\odot$ light curves can exceed L_γ. At and beyond core C burning, L_ν dominates the evolution of the $M \geqslant 8\ M_\odot$ light curves. Luminosities are normalized to $L_\odot = 3.828 \times 10^{33}$ erg s^{-1} (Prša et al. 2016).

Usually the ashes of nuclear burning have a larger $\overline{A}$ and lie interior to the unburned fuel. For example, a He core is interior to a H-burning shell, and a carbon–oxygen (CO) core is interior to a He-burning shell. Exceptions occur when electron degeneracy and thermal neutrino losses lead to a temperature inversion with cooler temperatures in the central regions and hotter temperatures exterior to the core. The fuel ignites off center and a burning front propagates toward the center.

For example, the $0.9\,M_\odot \leqslant M_{\rm ZAMS} \leqslant 2\,M_\odot$ light curves in Figure 2 undergo off-center He ignition, the He flash (Thomas 1967; Bildsten et al. 2012; Gautschy 2012; Serenelli et al. 2017). The accompanying nitrogen flash for neutrinos (Serenelli & Weiss 2005) are prominent and labeled. By contrast, the $M_{\rm ZAMS} \geqslant 2\,M_\odot$ light curves undergo central He burning. The $0.9\,M_\odot \leqslant M_{\rm ZAMS} \leqslant 7\,M_\odot$ light curves undergo TPs on the AGB, generating neutrinos first from H burning, and subsequently from He burning. A few light curves show a late TP during the transition to a cool WD.

Neutrino emission from nuclear reactions dominate whenever H and He burn; otherwise, neutrinos from thermal processes generally dominate (Farag et al. 2020). For example, light curves for $M_{\rm ZAMS} \geqslant 8\,M_\odot$ in Figure 2 have the minimum mass for C ignition and those for $M_{\rm ZAMS} \geqslant 10\,M_\odot$ have the minimum mass for Ne ignition (Becker & Iben 1979, 1980; García-Berro et al. 1997; Farmer et al. 2015; De Gerónimo et al. 2022). For these advanced burning stages L_ν in Figure 2 becomes nearly vertical and greatly exceeds L_γ. Thermal neutrinos from pair production dominate until the last few hours before CC when neutrinos from nuclear processes contribute (Odrzywolek et al. 2004; Odrzywolek & Heger 2010; Patton et al. 2017a, 2017b; Kato et al. 2020a, 2020b).

3.2. Six Metallicities

The top panel of Figure 3 shows the total energy emitted in photons E_γ and neutrinos E_ν, obtained by integrating L_γ and L_ν over the lifetime of a model. Metal-poor models tend to have larger E_γ and E_ν than the metal-rich models. Homology relations with power-law expressions for a bound–free Kramers opacity $\kappa \propto Z(1+X)\rho T^{-3.5}$, pp-chain energy generation rate $\epsilon_{\rm pp} \propto X^2 \rho T^4$, and mean molecular weight $\mu \propto X^{-0.57}$ lead to (Sandage 1986; Hansen et al. 2004)

$$E_\gamma \;\simeq\; L_\gamma\, \tau_{\rm MS} \propto (Z^{-1.1} X^{-5.0} M^{5.5})\, \tau_{\rm MS}, \tag{12}$$

where $\tau_{\rm MS}$ is the MS lifetime. Similarly, for a Thomson electron scattering opacity $\kappa \propto 1 + X$ and CNO cycle energy generation rate $\epsilon_{\rm CNO} \propto XZ\rho T^{17}$,

$$E_\gamma \;\simeq\; L_\gamma\, \tau_{\rm MS} \propto (Z^{-1.0} X^{-4.3} M^{5.1})\, \tau_{\rm MS}. \tag{13}$$

These expressions suggest that displacement on the MS due to a lower Z is partially offset by a shift to a larger X (Demarque 1960). In addition, a lower Z requires a higher $T_{\rm c}$ to produce the same L_γ and L_ν. This is mainly why the low-Z high-mass models in Figure 3 produce only a marginally larger L_γ and L_ν on the MS while possessing a larger $T_{\rm c}$. In turn, a larger L_γ implies a larger radiative gradient, and thus a larger core mass.

L_γ and L_ν in the core is primarily set by the mass of the model. Envelope opacities affect the rate of nuclear reactions in the core insofar as the envelope has a large mass. The hotter the model is overall (e.g., the more massive), the less mass in the envelope will be cold enough to provide bound–free or bound–bound opacity. The largest differences due to the opacity occur in the low-mass models because they are colder, both in the core and the envelope. The models adjust the structure to accommodate a change in Z at a fixed luminosity.

Overall, across the mass spectrum, metal-poor stellar models tend to have denser, hotter, and more massive cores with lower envelope opacities, larger surface luminosities, and larger effective temperatures $T_{\rm eff}$ than their metal-rich counterparts (Demarque 1960; Iben 1963; Demarque 1967; Iben & Rood 1970;

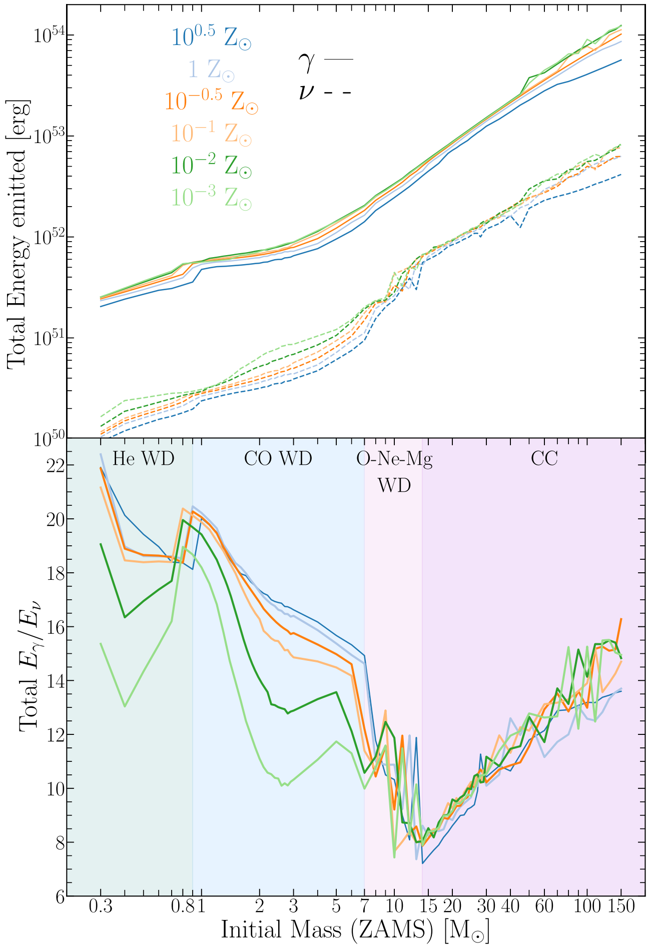

Figure 3. Total energy emitted in photons and neutrinos over the lifetime of a model (top) and their ratio (bottom) across the mass–metallicity plane. Transitions between different final fates occur at local extrema, indicated by the colored panels and labels.

Vandenberg 1983; Sandage 1986; Hansen et al. 2004; Georgy et al. 2013; Young 2018; Groh et al. 2019; Kemp et al. 2022). These are the main drivers of changes to the thermal and nuclear reaction neutrino emission as the initial Z changes.

The bottom panel of Figure 3 shows the ratio E_γ/E_ν. A maximum of $E_\gamma/E_\nu \simeq 20$ at $M_{\rm ZAMS} \simeq 0.9\,M_\odot$ occurs at the transition between models that ignite He and those that do not, between the most massive He WD and the least massive CO WD. As $M_{\rm ZAMS}$ increases, the resulting electron degenerate cores, first CO and then oxygen–neon–magnesium (ONeMg), become progressively more massive, denser, and hotter (also see Woosley & Heger 2015). This increases production of thermal neutrinos from the plasmon, photoneutrino, and pair annihilation channels faster than the production of reaction neutrinos or photons. Thus E_γ/E_ν decreases with $M_{\rm ZAMS}$ as shown in Figure 3.

A minimum of $E_\gamma/E_\nu \simeq 8$ at $M_{\rm ZAMS} \simeq 12\,M_\odot$ in Figure 3 occurs at the transition between models that produce the most massive WD and those that go to CC. As $M_{\rm ZAMS}$ further increases, thermal neutrinos from pair annihilation increase more slowly than reaction neutrinos or photons, and thus E_ν is smaller than E_γ in more massive models (pulsational pair-instability supernovae models are suppressed). The ratio E_γ/E_ν thus rises from the minimum and develops a roughly linear trend for $M_{\rm ZAMS} \gtrsim 12\,M_\odot$. Overall, both extrema of E_γ/E_ν of Figure 3 correlate with transitions in the final fate.

Another trend in the bottom panel of Figure 3 is the metallicity dependence of $M_{\rm ZAMS}$ models that become CO WD, the blue shaded region. More metal-rich models have a larger E_γ/E_ν than metal-poor models. A larger initial Z produces a larger accumulation of ^{14}N during CNO cycle H burning, thus a larger mass fraction of ^{22}Ne during He burning, and hence a smaller Y_e as the CO WD becomes more neutron-rich. Plasmon neutrino rates scale as Y_e^3, leading to a smaller E_ν; hence more metal-rich models have a larger E_γ/E_ν than metal-poor models in this $M_{\rm ZAMS}$ range. The dependence of CO WD on the ^{22}Ne mass fraction, the degree of neutronization, may have implications for the progenitor Type Ia supernova (Timmes et al. 2003; Townsley et al. 2009; Bravo et al. 2010; Piersanti et al. 2022) and the pulsation periods of variable WD (Campante et al. 2016; Chidester et al. 2021; Althaus & Córsico 2022).

Farag et al. (2020) showed $L_\gamma/L_\nu \simeq 40$ for a standard solar model. As this model evolves off the MS the inert He core becomes denser and more electron degenerate, the thermal neutrino production rises, L_ν increases, and thus L_γ/L_ν decreases. Integrated over the lifetime of the model, E_γ/E_ν decreases to $\simeq$20, as shown in Figure 3.

For any $M_{\rm ZAMS}$, what is the impact of changing Z on the neutrino emission at any evolutionary stage?

Figure 4 compares L_ν to L_ν of the $Z = 1\,Z_\odot$ model across the mass–metallicity plane at three evolutionary stages in the top three panels. As for Figure 3, at the ZAMS there is generally a small dependence on the initial Z, but there are interesting features. For example, the dip at $M_{\rm ZAMS} \simeq 1.2\,M_\odot$ corresponds to the transition from pp-chain dominated to CNO cycle dominated H burning. Another feature is the stronger Z dependence for $M_{\rm ZAMS}$ models that become CO WDs. As low-Z models tend to have denser, hotter, and more massive H-burning cores, thermal and reaction neutrino contributions to L_ν are larger relative to high-Z models.

At the TAMS, the $0.2\,M_\odot \leqslant M_{\rm ZAMS} \leqslant 8.0\,M_\odot$ models in Figure 4 have a partially degenerate He-rich core. As low-Z models have denser, hotter, and more massive cores than high-Z models, the thermal plasmon neutrino contributions to L_ν are larger. More massive $M_{\rm ZAMS}$ models do not develop degenerate He-rich cores, and the small dependence on the initial Z continues. The most metal-rich track decreases due to the larger mass loss.

At core He depletion (CHeD), the $0.9\,M_\odot \leqslant M_{\rm ZAMS} \leqslant 8.0\,M_\odot$ models have a partially electron degenerate CO-rich core. The denser, hotter, and more massive cores of the low-Z models means larger thermal neutrino contributions, and thus L_ν is larger in lower-Z models.

The $M_{\rm ZAMS} \geqslant 60\,M_\odot$ models at CHeD in Figure 4 show sawtooth profiles, with the lowest-Z models disrupting a metallicity trend. This occurs because the convective boundary mixing model, exponential overshooting (Herwig 2000), is based on the pressure scale height $H = P/(\rho g) \simeq k_{\rm B}T/(\mu_{\rm ion} g)$, where P is the pressure, $k_{\rm B}$ is the Boltzmann constant, and g is the gravitational acceleration. All else being equal, a smaller Z means a smaller $\mu_{\rm ion}$, a larger H, and thus the chemical mixing region in low-Z models is larger than in high-Z models. If two burning shells are within H, they are mixed. For masses with low L_ν, the H shell mixes into the burning He core repeatedly. This delays core He burning until there is a homogeneous

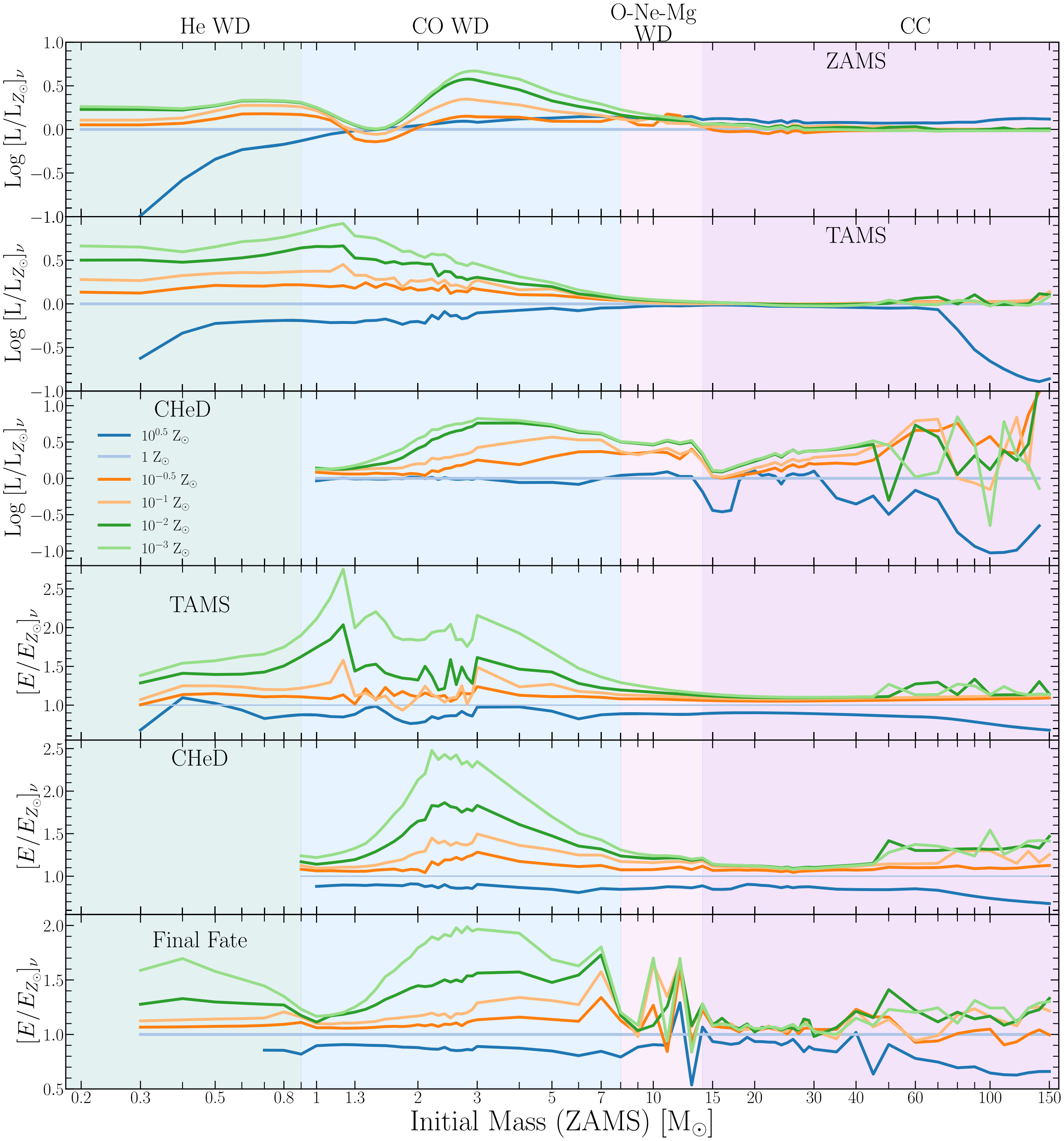

Figure 4. Ratio of L_ν to L_ν of the $Z = 1\ Z_\odot$ model vs. $M_{\rm ZAMS}$ for all six metallicities at ZAMS (top panel), TAMS (second panel), and core He depletion (CHeD; third panel). The ratio of E_ν to E_ν of the $Z = 1\ Z_\odot$ model versus $M_{\rm ZAMS}$ for all six metallicities at TAMS (fourth panel), CHeD (fifth panel), and final fate (bottom panel). Each panel is colored by the final fate given by the legend.

stripped CO core with a little He on the surface. By CHeD, there is no H shell to undergo CNO burning and all the ^{14}N is depleted, ergo L_ν is very low.

Overall, for fixed overshooting parameters, metal-poor models have larger amounts of chemical mixing. This is a secondary driver of changes to the thermal and nuclear reaction neutrino emission as the initial metallicity changes. Other specific examples of overshooting dominating are shown for low-mass models in Section 4 and for high-mass models in Section 5. The overshooting prescription may have an additional metallicity dependence that is not captured by these models.

Figure 4 also compares E_ν at each $M_{\rm ZAMS}$ to E_ν of the $Z = 1\ Z_\odot$ model on a linear scale at three evolutionary stages in the bottom three panels. At the TAMS, models across the mass spectrum reflect the Z dependence of L_ν shown in the top two panels. At CHeD, the denser, hotter, and more massive cores of the low-Z models, plus contributions from the conversion of ^{14}N into ^{22}Ne, also show larger E_ν with decreasing Z.

Tracks in the bottom panel of Figure 4 are the same neutrino tracks in Figure 3 but normalized to the solar metallicity track. The $M_{\rm ZAMS}$ range for He WDs and CO WDs have the metallicity signature of having had an inert, electron degenerate core during their evolution. The ONeMg WD region shows a sawtooth pattern because these models had numerical challenges completing the propagation of their off-center, convectively bounded flame fronts to the center. The $M_{\rm ZAMS}$ region for CC events shows a weak dependence of E_ν on Z.

4. Low-mass Stars

Here, we analyze the neutrino emission from the low-mass stellar tracks at one metallicity in Section 4.1, and then for all six metallicities in Section 4.2.

4.1. One Metallicity

Figure 5 shows the $0.2\,M_\odot \leqslant M_{\rm ZAMS} \leqslant 7.0\,M_\odot$ tracks in a γHRD and a νHRD for $Z = 1\,Z_\odot$. The cores are progressively enriched with the ashes of H burning as the models begin to evolve beyond the MS. The H-burning reactions increase μ and thus ρ in the core. To maintain hydrostatic equilibrium the central temperature $T_{\rm c}$ rises with the central density $\rho_{\rm c}$, increasing the rate of nuclear fusion and thus L_γ and L_ν. This slow increase of $T_{\rm c}$ is reflected in the γHRD and νHRD of Figure 5 as an increase in their respective luminosities until core H depletion at the TAMS.

The He-rich core contracts as a H-burning shell forms and the tracks in Figure 5 evolve across both HRDs on a thermal timescale. Both L_γ and L_ν increase along the RGB until core He ignition at the tip of the RGB. All tracks that reach this point have a semi–electron degenerate He core with $0.5\,M_\odot \leqslant M_{\rm He} \leqslant 1.7\,M_\odot$, and a similar L_γ, L_ν, and $T_{\rm eff}$ (Cassisi & Salaris 2013; Serenelli et al. 2017). Photons from the tip of the RGB provide a standard candle distance indicator (Da Costa & Armandroff 1990; Lee et al. 1993; Madore et al. 2023) and offer constraints on the neutrino magnetic dipole moment (Capozzi & Raffelt 2020; Franz et al. 2023).

He ignition by the triple-α process in the $0.9\,M_\odot \leqslant M_{\rm ZAMS} \leqslant 2.1\,M_\odot$ tracks of Figure 5 occur off center (on center in the $2.1\,M_\odot$) and under semi–electron degenerate conditions in a helium flash (Thomas 1967; Bildsten et al. 2012; Gautschy 2012; Serenelli et al. 2017). A He-burning front propagates toward the center by conduction, with burning behind the front driving convection. The helium flash and the subflashes that follow burn very little He; the nuclear energy generated mainly goes into lifting the electron degeneracy in the core. The last subflash reaches and heats the center, allowing stable convective core He burning under nondegenerate conditions.

During each helium flash, a nitrogen flash also occurs from the conversion of all of the accumulated ^{14}N to ^{22}Ne, sharply increasing L_ν via ^{18}F($,e^+\nu_e$)^{18}O (Serenelli & Weiss 2005). For example, Figure 6 shows that an $M_{\rm ZAMS} = 1\,M_\odot$, $Z = 1\,Z_\odot$ track undergoes seven flashes. The first flash is the strongest, occurring at $M \simeq 0.2\,M_\odot$ and reaches $L_\nu \simeq 2 \times 10^7\,L_\odot$ for $\simeq$3 days.

Tracks with $M_{\rm ZAMS} \geqslant 2.1\,M_\odot$ reach a high enough $T_{\rm c}$ at the tip of the RGB to ignite He in the center quiescently under nondegenerate conditions. For example, Figure 6 shows an $M_{\rm ZAMS} = 3\,M_\odot$, $1\,Z_\odot$ track produces a smoother L_ν signature during core He burning than an $M_{\rm ZAMS} = 1\,M_\odot$, $1\,Z_\odot$ track. Tracks in this mass–metallicity range also experience a blue loop (Hayashi et al. 1962; Hofmeister et al. 1964; Xu & Li 2004; Zhao et al. 2023) in the γHRD and νHRD of Figure 5.

Post He ignition, the tracks in Figure 5 migrate to the horizontal branch (HB), becoming less luminous with larger $T_{\rm eff}$. All the He cores have approximately the same mass, regardless of the total stellar mass, and thus about the same helium fusion luminosity $L_{\rm He}$. These stars form the red clump at $T_{\rm eff} \simeq 5000$ K, $L_\gamma \simeq 50\,L_\odot$, and $L_\nu \simeq 20\,L_\odot$ (Alves & Sarajedini 1999; Girardi 1999; Sarajedini 1999; Hawkins et al. 2017; Wang & Chen 2021). Less-massive H envelopes shift the tracks to hotter $T_{\rm eff}$ and smaller L_γ on the HB. This effect occurs more readily at lower Z (see Section 4.2) with old metal-poor clusters showing pronounced HBs in a γHRD (Casamiquela et al. 2021; Dondoglio et al. 2021).

Core He burning produces an electron degenerate CO core with a semi electron degenerate He shell encased in a larger H-rich envelope. These AGB stars are the final stage of evolution driven by nuclear burning, characterized by H and He burning in geometrically thin shells on top of the CO core (Herwig 2005). Larger $M_{\rm ZAMS}$ yield super-AGB models, where an ONeMg core forms from a convectively bounded carbon flame propagating toward the center (Becker & Iben 1979, 1980; Timmes et al. 1994; García-Berro et al. 1997; Siess 2007; Denissenkov et al. 2015; Farmer et al. 2015; Lecoanet et al. 2016).

During the AGB phase, a thin He shell grows in mass as material from the adjacent H-burning shell is processed, causing the He shell to increase in temperature and pressure. When the mass in the He shell reaches a critical value (Schwarzschild & Härm 1965; Giannone & Weigert 1967; Siess 2010; Gautschy 2013; Lawlor 2023), He ignition causes a thermal pulse (TP).

For example, Figure 6 shows the L_ν of a $3\,M_\odot$, $1\,Z_\odot$ track experiencing a series of 21 TPs, with an interpulse period of $\simeq 10^5$ yr. Like the helium flash, each TP is composed of a primary flash followed by a series of weaker subflashes. These TP sequences appear as spikes in the νHRD of Figure 5. The primary flash produces the largest $L_\nu \simeq 4.6 \times 10^4\,L_\odot$ from ^{18}F($,e^+\nu_e$)^{18}O. The subflashes do not produce neutrino emissions from this process, as nearly all of the ^{14}N is converted to ^{22}Ne during the primary flash. The number of TPs a track undergoes is uncertain, as the number is sensitive to the mass and time resolution, the stellar mass-loss rate, and the treatment of convective boundaries.

4.2. Six Metallicities

Figure 7 shows the evolution of $M_{\rm ZAMS} = 1\,M_\odot$ and $3\,M_\odot$ in a γHRD and a νHRD across all six metallicities. Overall, the low-Z models show the trend of having denser, hotter, and more massive cores with lower envelope opacities, larger surface luminosities, and larger effective temperatures $T_{\rm eff}$ than the high-Z counterparts. Features in the νHRD between core H depletion and the end of the TP-AGB phase are analyzed below.

The tracks in Figure 7 leave the TP-AGB phase when the envelope mass above the H- and He-burning shells is reduced to $\simeq$0.01 $M_\odot$ by stellar winds. All the tracks then evolve toward larger $T_{\rm eff}$ at nearly constant L_ν and L_γ. The $M_{\rm ZAMS} = 1\,M_\odot$ and $3\,M_\odot$ tracks, in both the γHRD and νHRD, show late TPs for some metallicities. These are the result of a strong He flash (and nitrogen flash) that occurs after the AGB phase but before the WD cooling phase (Iben et al. 1983; Bloecker & Schoenberner 1997; Lawlor 2023). A candidate late TP star is V839 Ara, the central star of the Stingray Nebula (Reindl et al. 2017; Peña et al. 2022). The more dramatic very late TP stars, also visible in Figure 7, include Sakurai's Object, V605

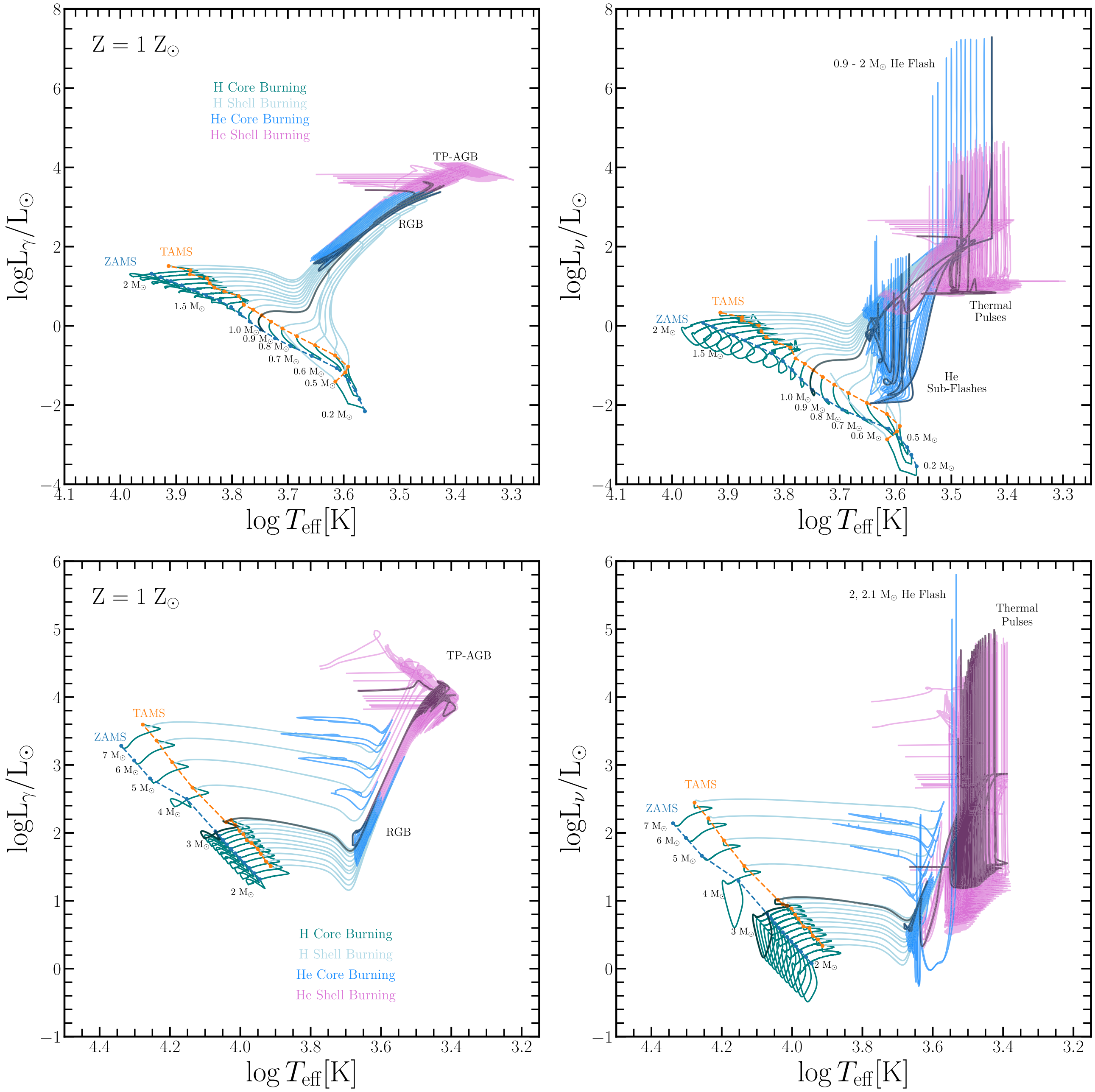

Figure 5. Low-mass tracks in a γHRD (left panels) and a νHRD (right panels) for $Z = 1\ Z_\odot$ over 0.2–2.0 $M_\odot$ (top row) and 2.0–7.0 $M_\odot$(bottom row). Tracks are colored by evolutionary phase and labeled. WD cooling tracks are suppressed for visual clarity. Luminosities are normalized to $L_\odot = 3.828 \times 10^{33}$ erg s^{-1} (Prša et al. 2016). The 1 $M_\odot$ and 3 $M_\odot$ tracks are highlighted in black as they are analyzed in detail as examples of low-mass models that do and do not undergo the He flash, respectively.

Aql, and perhaps HD 167362, the central star of planetary nebula SwSt 1 (Clayton & De Marco 1997; Herwig 2002; Miller Bertolami & Althaus 2007; Hajduk et al. 2020; Lawlor 2023).

Plasmon neutrino emission then dominates the energy-loss budget in Figure 7 for average-mass $\simeq$0.6 $M_\odot$ CO WDs with $T_{\rm eff} \gtrsim$25,000 K (Vila 1966; Kutter & Savedoff 1969; Bischoff-Kim & Montgomery 2018). As the WD continues to cool, photons dominate the cooling as the electrons transition to a strongly degenerate plasma (van Horn 1971; Córsico et al. 2019). The tracks in Figure 7 are arbitrarily chosen to terminate when the WD reaches $L \leqslant 10^{-3} L_\odot$. This is sufficient (see Figure 5 of Timmes et al. 2018) for calculating the integrated neutrino background from a simple stellar population.

Figure 8 shows the fraction of L_ν from specific reaction sequences and weak reactions over the lifetime of the 1 $M_\odot$ models for all six metallicities. Fractions whose components do not sum to unity indicate the contribution of thermal neutrinos to L_ν.

The green shaded regions correspond to shell H burning. The fraction of L_ν from the CNO cycles in this phase steadily increases with metallicity from $Z = 10^{-3}\ Z_\odot$ in the bottom panel to $Z = 10^{0.5}\ Z_\odot$ in the top panel. Since the CNO nuclei catalyze H burning, L_γ and L_ν depend directly on the initial metallicity.

The blue shaded regions represent core He burning. In this phase, the fraction of L_ν from the ^{19}F $\rightarrow$ ^{18}O reaction dominates during the nitrogen flash. Neutrino emission from

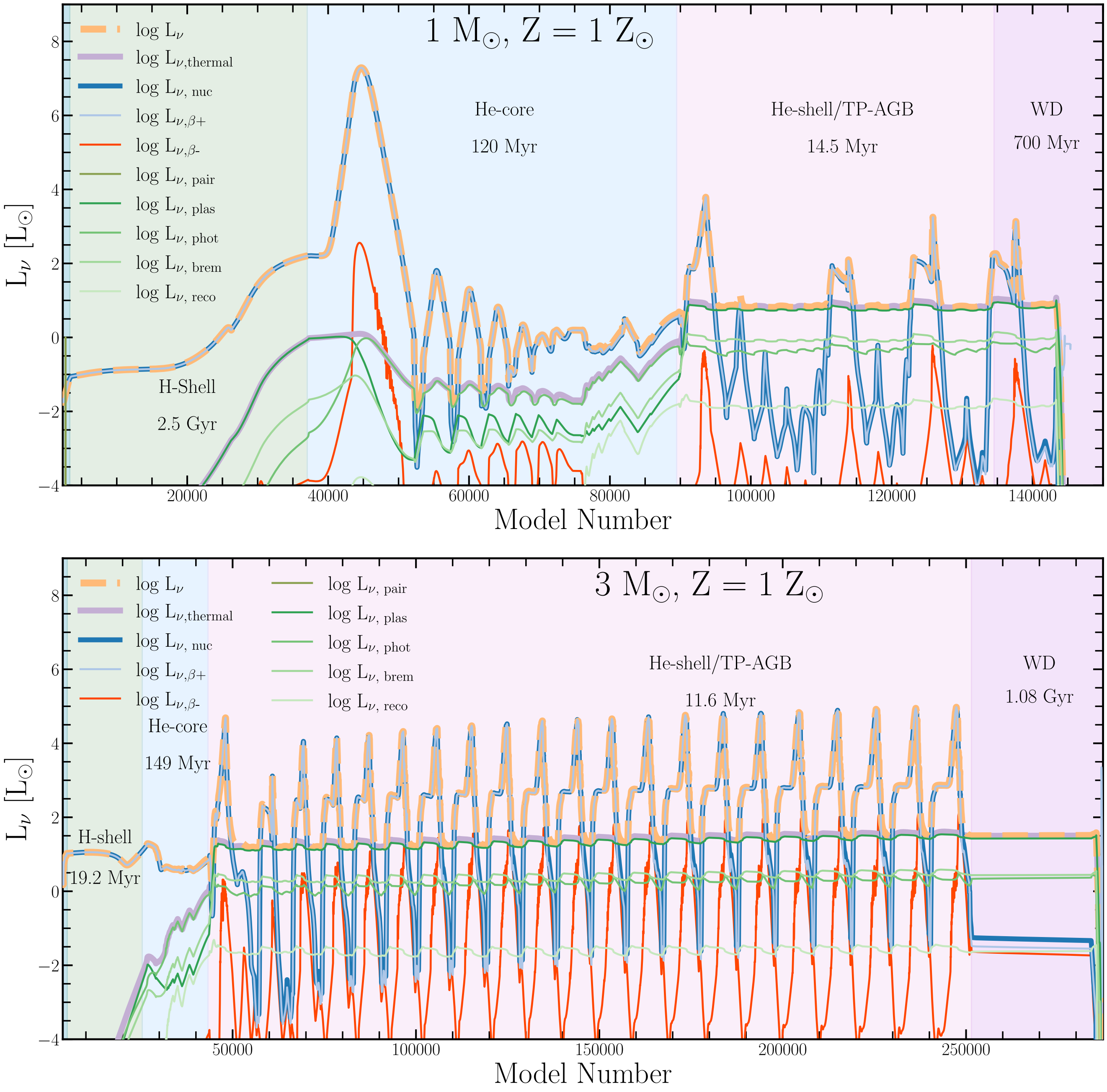

Figure 6. Components of L_ν over the lifetimes of a 1 $M_\odot$, 1 $Z_\odot$ model (top) and a 3 $M_\odot$, 1 $Z_\odot$ model (bottom). The *x*-axis is the sequential model number, a nonlinear proxy for time, which begins on the left at core H depletion and ends on the right as a cool WD at each metallicity. Phases of evolution are marked by the colored regions, and the time spent in each phase is labeled. Curves show the luminosities from nuclear and thermal processes and their subcomponents, and are smoothed with a 50 model moving-average filter. Luminosities are normalized to $L_\odot = 3.828 \times 10^{33}$ erg s^{-1} (Prša et al. 2016).

the H-burning pp-chain and CNO cycles appear during this phase of evolution for all six metallicities due to convective boundary mixing processes ingesting fresh H-rich material into the hotter core region. For the $Z \geqslant 10^{-0.5}$ $Z_\odot$ tracks, the convective boundary mixing processes and hotter temperatures drive the H-burning Mg–Al cycles (red curves) and the appearance of $^{26}\mathrm{Al} \rightarrow {}^{26}\mathrm{Mg}$ between subflashes.

Shell He burning and the TP-AGB phase of evolution are shown by the pink shaded regions in Figure 8. The $Z = 10^{-1,-0.5,0}$ $Z_\odot$ tracks show traditional TPs, with the fractions contributing to L_ν oscillating between successive TPs. Neutrino emission is initially from CNO burning before a TP, and then from $^{19}\mathrm{F} \rightarrow {}^{18}\mathrm{O}$ during the ensuing He-burning TP.

The $Z = 10^{-3}$ $Z_\odot$ and $Z = 10^{-2}$ $Z_\odot$ tracks in Figure 8 do not show traditional TPs. Instead they show a single event from a merger of their H shells and He shells that is driven by convective boundary mixing. As analyzed in Section 3.2, this is because metal-poor models have larger chemical convective boundary mixing regions than metal-rich models for fixed overshooting parameters. The $Z = 10^{0.5}$ $Z_\odot$ tracks in Figure 8 also do not show traditional TPs due their thinner envelopes, caused by the metallicity dependent line-driven wind mass-loss prescriptions removing more envelope mass ($\dot{M} \propto Z$). During the WD cooling phase (purple shaded regions), late TPS are visible in the $Z = 10^{-1,0}$ $Z_\odot$ tracks by the rise of L_ν from CNO burning and subsequently $^{19}\mathrm{F} \rightarrow {}^{18}\mathrm{O}$.

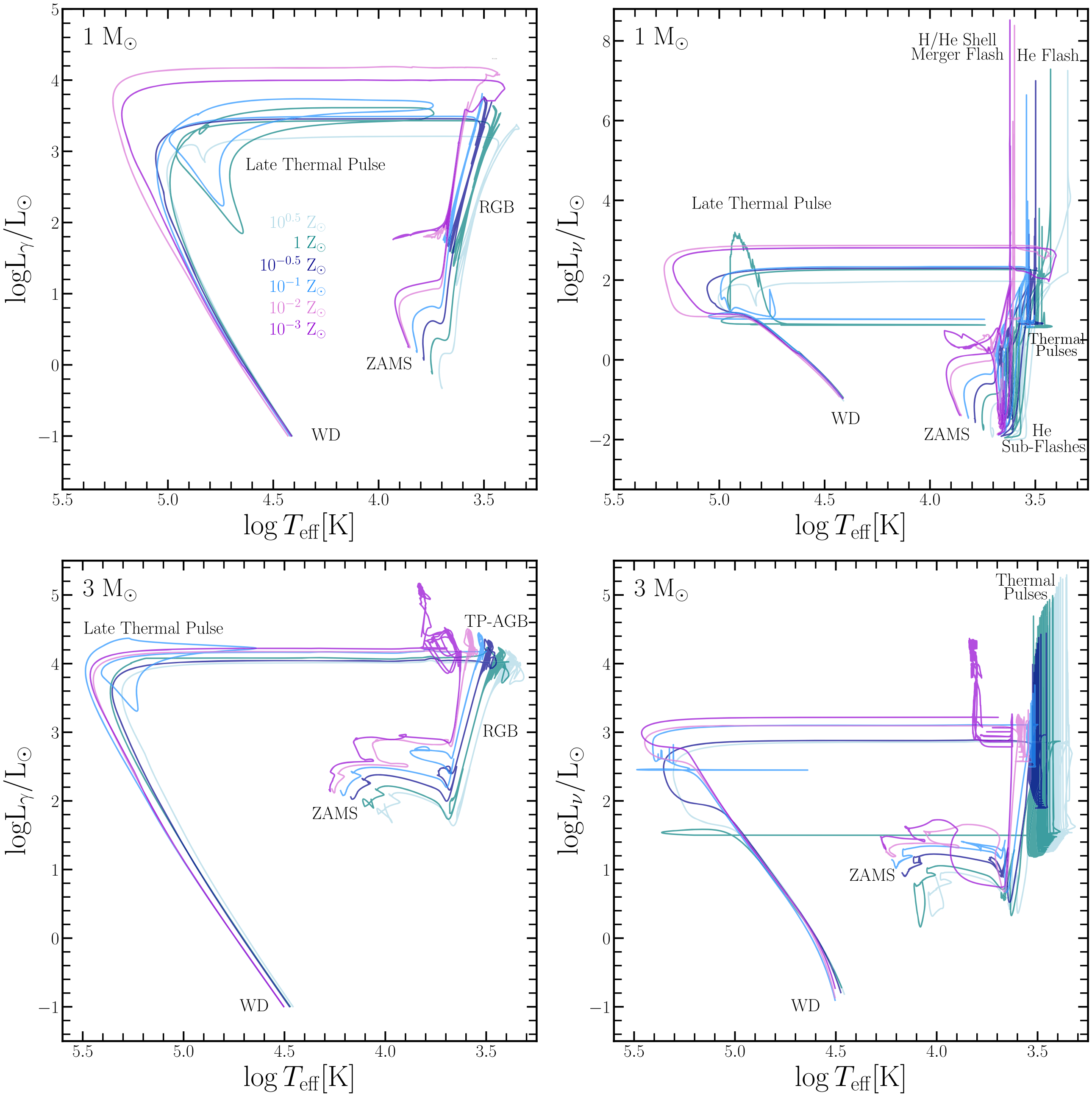

Figure 7. Tracks in a γHRD (left panels) and νHRD (right panels) for $M_{\rm ZAMS} = 1\ M_\odot$ (top row) and $3\ M_\odot$ (bottom row) across all six metallicities. Luminosities are normalized to the current solar photon luminosity $L_\odot = 3.828 \times 10^{33}$ erg s^{-1} (Prša et al. 2016). Metal-poor tracks are generally bluer and more luminous than metal-rich tracks.

Figure 9 is the same as Figure 8 but for the lifetime of the $3\ M_\odot$ models for all six metallicities. The fraction of L_ν from CNO processing during shell H burning (green regions) is larger for the $3\ M_\odot$ tracks than the corresponding $1\ M_\odot$ tracks of Figure 8 at all metallicities. Core He burning (blue shaded regions) proceeds smoothly under nondegenerate conditions at all metallicities. The spikes from ^{19}F → ^{18}O in the $Z = 10^{0.5}\ Z_\odot$ track during core He burning are due to overshooting injecting fresh H-rich fuel into the core. Shell He burning and the TP-AGB phase of evolution (pink regions) show a trend of stronger and more numerous TPs as the metallicity increases from $Z = 10^{-3}\ Z_\odot$ to $Z = 10^{0.5}\ Z_\odot$. Hotter temperatures in the $3\ M_\odot$ models cause neutrino emission from ^{26}Al → ^{26}Mg during the H-burning Ne–Na cycle (red curves) and from the inverse-beta decay ^{24}Na → ^{24}Mg reaction (purple curves). While ^{24}Na is not part of the H-burning Mg–Al cycle, this isotope is synthesized at low abundance levels during the Mg–Al cycle. A late TP occurs during the WD cooling phase (purple regions) for the $Z = 10^{0,-1}\ Z_\odot$ tracks.

Figure 10 shows L_ν, L_γ, and the He-burning luminosity $L_{\rm He}$ during the nitrogen flash in $1\ M_\odot$ models. Across all metallicities the first flash has the largest L_ν and $L_{\rm He}$, with $L_{\rm He} > L_\nu$. The maximum neutrino luminosity $L_{\nu,\rm max}$, marked by the red circles and labels, spans $\simeq$2 orders of magnitude as the initial metallicity varies from $Z = 10^{-3}\ Z_\odot$ to $Z = 10^{0.5}\ Z_\odot$. Note that $L_{\nu,\rm max}$ is larger for the $Z = 1\ Z_\odot$ model than for the $Z = 10^{0.5}$ model. This is due to mass loss. If the metallicity was $10^{0.3}\ Z_\odot$, then $L_{\nu,\rm max}$ at the He flash would be larger than for the $Z = 1\ Z_\odot$ model. At $Z = 10^{0.5}\ Z_\odot$, mass loss hampers the strength

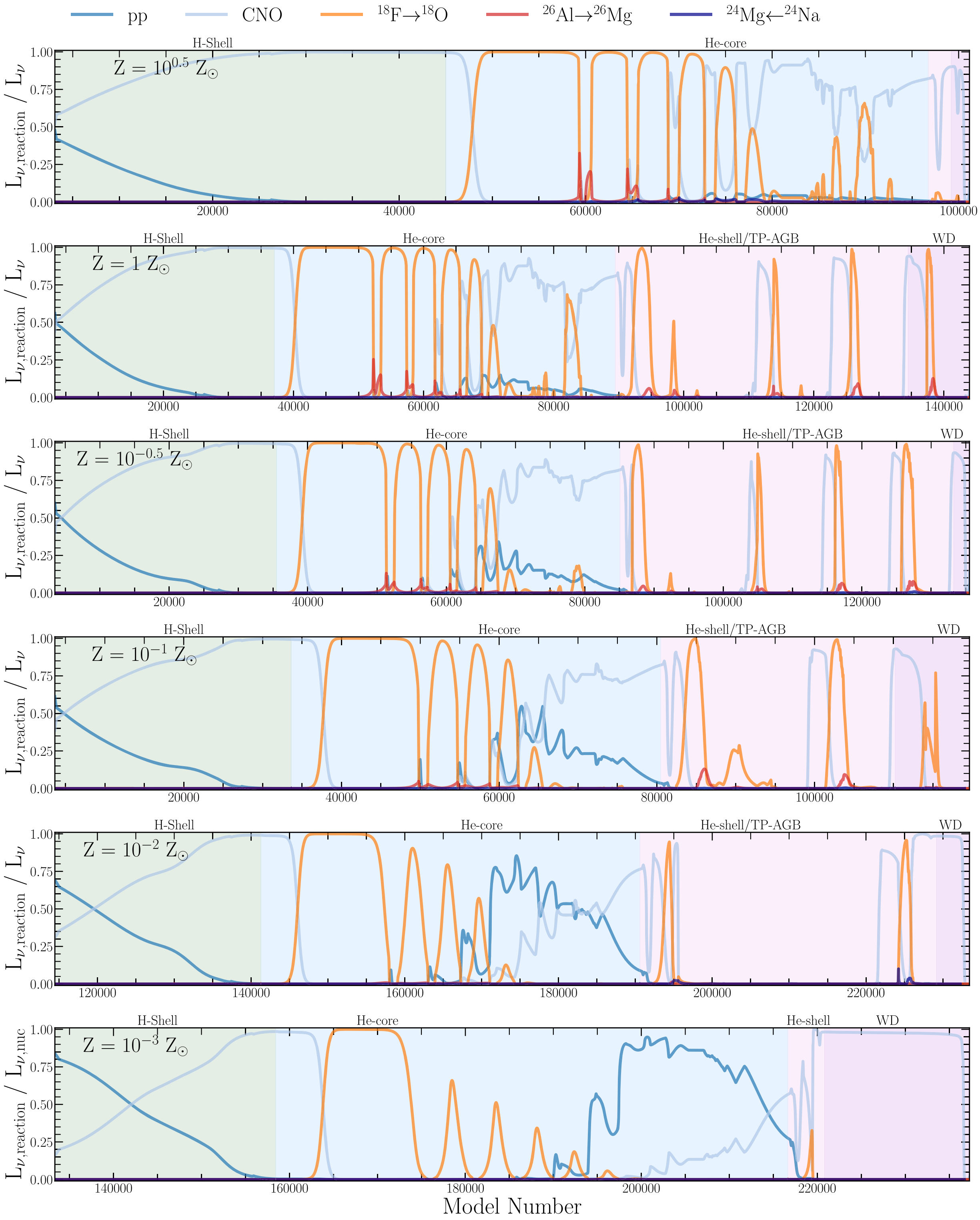

Figure 8. Components of L_ν from nuclear reactions over the lifetime of an $M_{\rm ZAMS} = 1\ M_\odot$ model for all six metallicities. The *x*-axis is the sequential model number, a proxy for time, beginning at core H depletion (left) and ending as a cool WD (right). Curves are smoothed with a 50 model moving-average filter. Evolutionary phases are shown by the colored regions and labeled. Reactions emitting neutrinos in the pp-chain and CNO cycles are listed in Section 3.1.

of the He flash. The $Z = 10^{0.5}\ Z_\odot$ model has $M = 0.6\ M_\odot$ at the onset of the He flash, while the $Z = 1\ Z_\odot$ model has $M = 0.66\ M_\odot$. The smaller shell-burning temperatures are sufficient to weaken $L_{\nu,\max}$. Note that the duration of the peak in the $Z = 10^{0.5}\ Z_\odot$ model is significantly longer than in the $Z = 1\ Z_\odot$ model, ensuring more neutrinos are produced overall from the larger ^{14}N reservoir, but with an $L_{\nu,\max}$ of similar magnitude.

Figure 10 shows the average neutrino energy at $L_{\nu,\max}$ is insensitive to the initial Z. The neutrino fluxes at $L_{\nu,\max}$ span $\simeq$2 orders of magnitude across metallicity and can serve as target values for neutrino observations of the nitrogen flash.

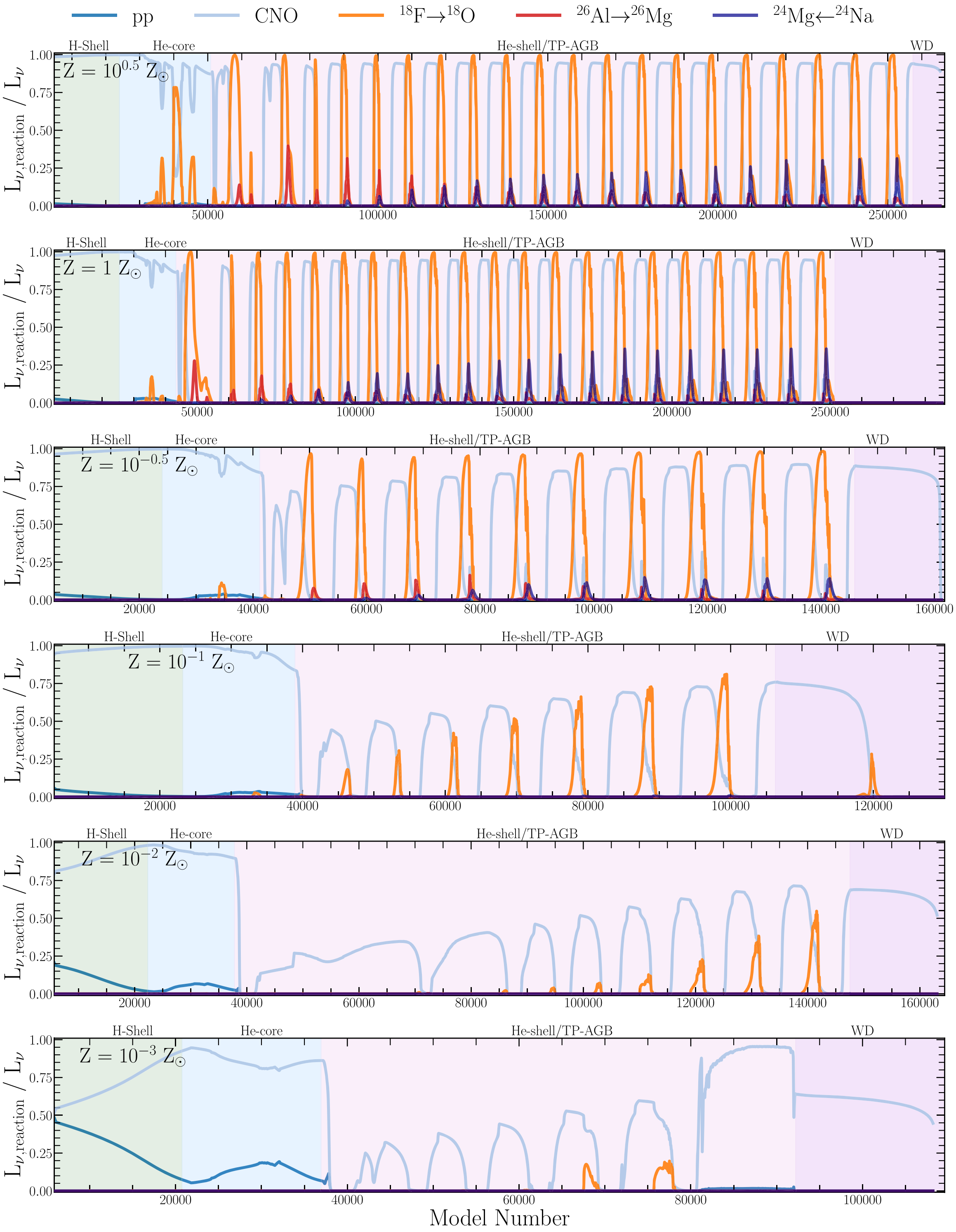

Figure 9. Same as Figure 8 but for 3 $M_\odot$ models.

The duration where $L_\nu \geqslant 1/2\ L_{\nu,\max}$ increases steadily from ≃0.8 days at $Z = 10^{-3}\ Z_\odot$ to ≃11 days at $Z = 10^{0.5}\ Z_\odot$. The duration where $L_\nu \geqslant 1/3\ L_{\nu,\max}$ increases from ≃1.2 days at $Z = 10^{-3}\ Z_\odot$ to ≃17 days at $Z = 10^{0.5}\ Z_\odot$. In addition, the time period between subflashes increases from $\simeq 10^5$ yr at $Z = 10^{-3}\ Z_\odot$ to $\simeq 2 \times 10^5$ yr at $Z = 10^{0.5}\ Z_\odot$, while the number of subflashes ranges between eight at the lowest initial Z to five at the largest initial Z.

Figure 11 shows L_ν, L_γ, and L_{He} during the TP-AGB phase of evolution in 1 $M_\odot$ models for all six metallicities. As discussed for Figure 8, the tracks for the lowest initial Z show a single H-shell and He-shell merger event instead of a traditional TP. For these models L_ν is dominated by $^{13}\mathrm{N} \rightarrow {}^{13}\mathrm{C}$ from nonequilibrium hot CNO cycle burning. At the peak of the merger $T \simeq 2 \times 10^8$ K and $\rho \simeq 10^4$ g cm^{-3}. At these conditions, the first half of the CNO cycle, $^{12}\mathrm{C}(p,\gamma)^{13}\mathrm{N}(,e^+\nu)^{13}\mathrm{C}(p,\gamma)^{14}\mathrm{N}$, is sufficiently energetic to cause a rapid expansion that self-quenches the second half of the CNO cycle, $^{14}\mathrm{N}(p,\gamma)^{15}\mathrm{O}(,e^+\nu)^{15}\mathrm{N}(p,\alpha)^{12}\mathrm{C}$. For example, the stellar radius R of the $Z = 10^{-3}\ Z_\odot$ model rapidly increases from 68 $R_\odot$ to 465 $R_\odot$ during the merger, and the number of reactions

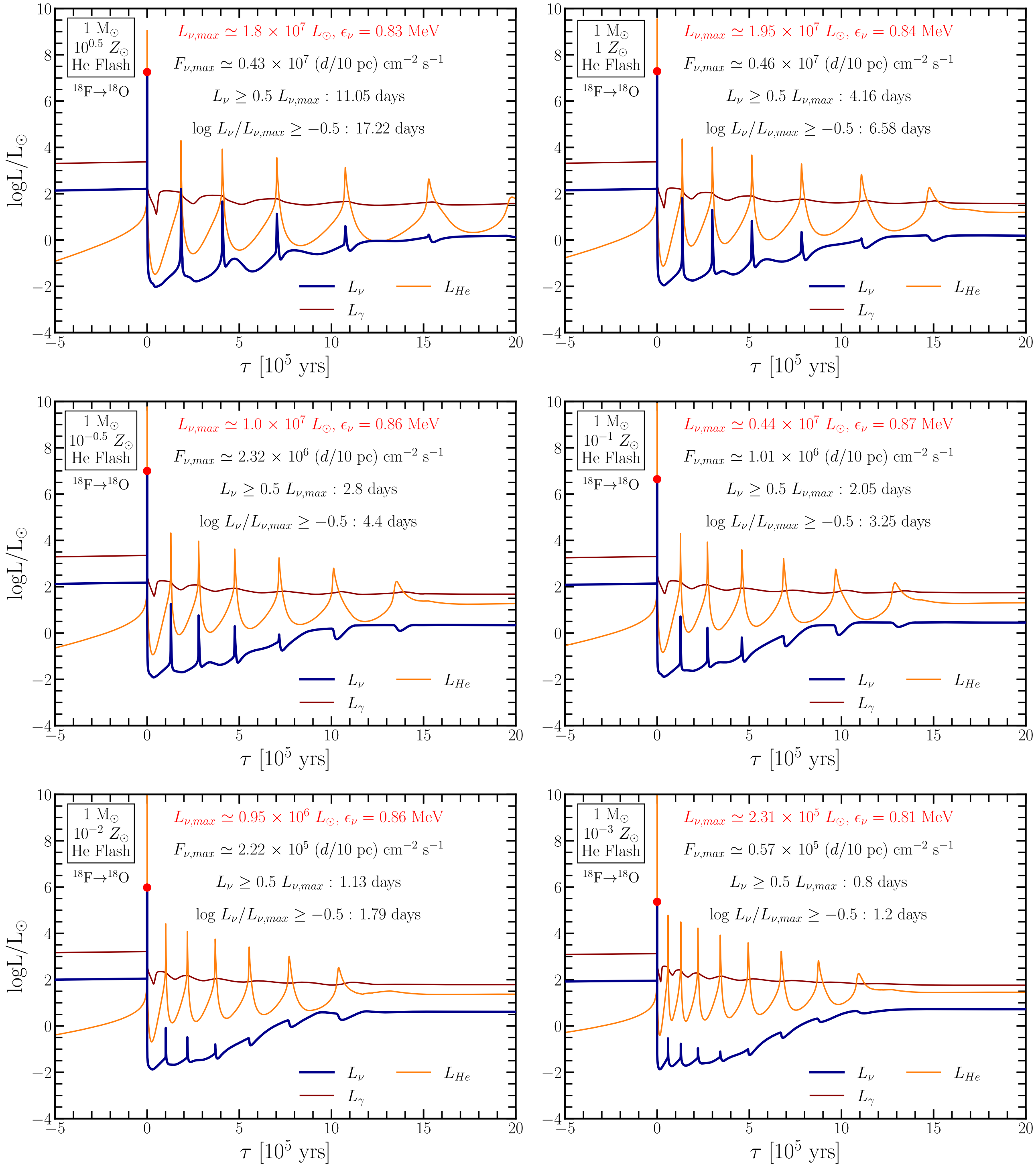

Figure 10. Neutrino targets for the nitrogen flash in 1 $M_\odot$ models for all six metallicities. The x-axis is the time since the first, and strongest, nitrogen flash. The y-axis is a luminosity relative to $L_\odot = 3.828 \times 10^{33}$ erg s^{-1} (Prša et al. 2016). Colored curves show the ν, γ, and He-burning luminosity. The red circle marks the maximum L_ν, and the red label gives the value of $L_{\nu,\mathrm{max}}$ and the average neutrino energy. Labeled are the maximum flux at a distance d in parsecs, and the duration for the L_ν to be larger than 1/2 and 1/3 $L_{\nu,\mathrm{max}}$. Metal-rich models have larger $L_{\nu,\mathrm{max}}$ and longer periods between flashes.

per second from ^{13}N → ^{13}C is ≃3 orders of magnitude larger than from ^{15}O → ^{15}N. Thus, these 1 $M_\odot$ low-Z models do not undergo a TP because a violent shell merger causes the model to quickly lose most of the H envelope. These mergers, driven by convective boundary mixing, produce the largest $L_{\nu,\mathrm{max}}$ events over the entire evolution. They are also prominent and labeled in the νHRD of Figure 7. The $Z = 10^{0.5}\ Z_\odot$ track also does not show TPs due to their thinner envelopes from wind mass loss. For the other metallicities, $L_{\nu,\mathrm{max}}$ during the TPs is ≃3 orders of magnitude smaller than $L_{\nu,\mathrm{max}}$ from the nitrogen flash shown in Figure 10.

Figure 12 shows L_ν, L_γ, and L_{He} during the TP-AGB phase in the 3 $M_\odot$ models. The number of L_ν peaks (6 to 21), the L_ν peaks ($2 \times 10^3\ L_\odot$ to $2 \times 10^5\ L_\odot$), and time between L_ν peaks (2×10^4 to 4×10^4 yr) increase with Z, with evidence of saturation by $Z = 1\ Z_\odot$. Each successive TP releases more nuclear energy, and thus $L_{\nu,\mathrm{max}}$ occurs at the end of

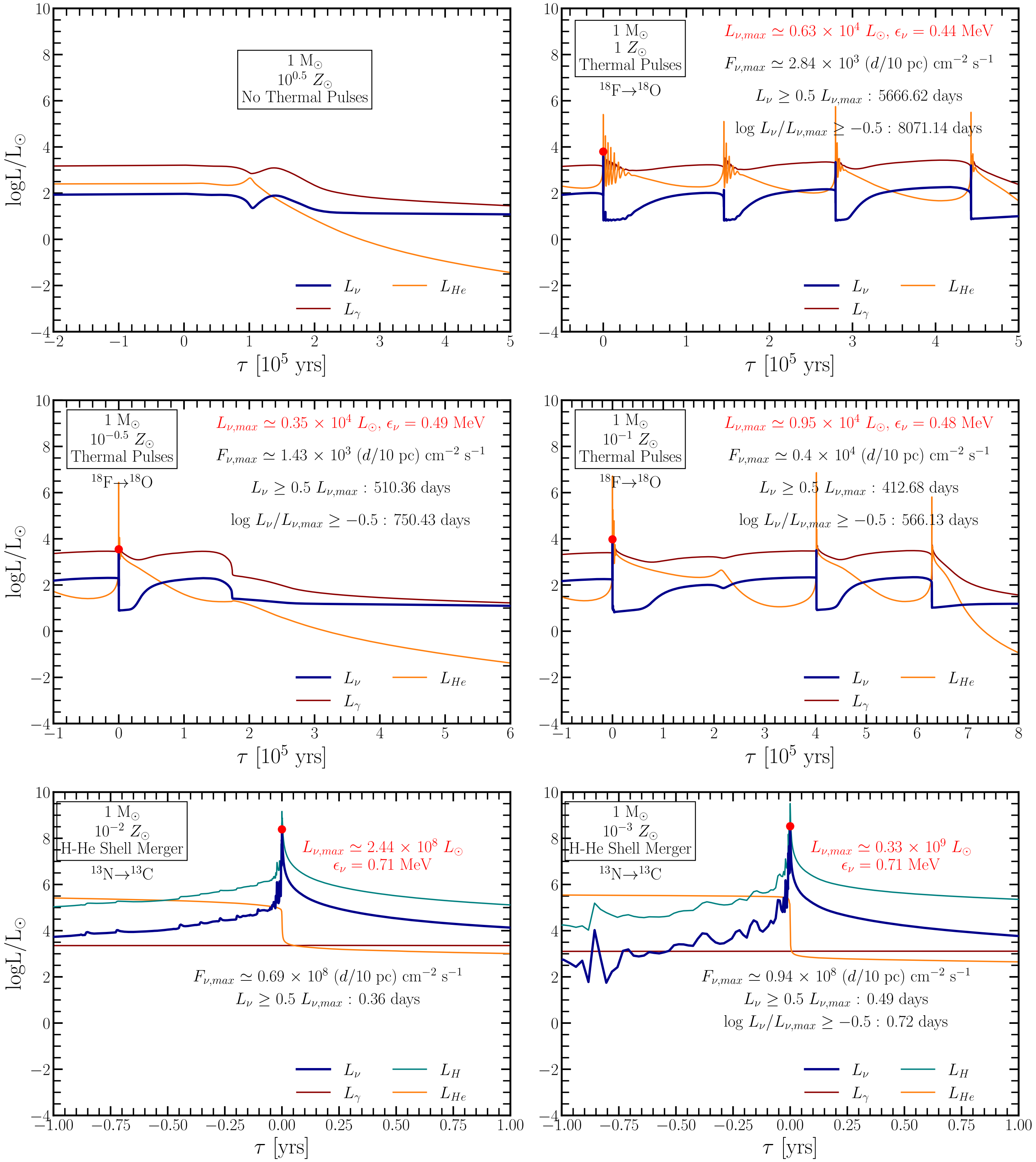

Figure 11. Same format as Figure 10 but for the TP-AGB phase of evolution.

the tracks (red circles and labels) across all metallicities. The $Z = 10^{-3}\,Z_\odot$ model has a larger $L_{\nu,\mathrm{max}}$ than the $Z = 10^{-2}\,Z_\odot$ model due to $^{13}\mathrm{N} \rightarrow {}^{13}\mathrm{O}$ (instead of the usual $^{18}\mathrm{F} \rightarrow {}^{18}\mathrm{O}$) from a shell merger that is driven by convective boundary mixing.

Figure 13 compares the fraction of the total energy emitted by neutrinos at five phases of evolution across the mass–metallicity plane. Models with $0.2\,M_\odot \leqslant M_{\mathrm{ZAMS}} \leqslant 0.8\,M_\odot$ emit ≃80% of their neutrinos during shell H burning (second panel) with a slight trend toward high-Z tracks making larger contributions than low-Z tracks. A ≃10% contribution originates from core H burning (top panel), and a ≃10% contribution occurs during the He WD cooling phase (bottom panel). These models do not go through a shell He-burning phase, as indicated by the empty region in the fourth panel, and the shorter tracks in the γHRD and νHRD of Figure 7.

Models whose final fate is a CO WD emit ≃20%–80% of their neutrinos during core H burning, ≃20%–40% during core

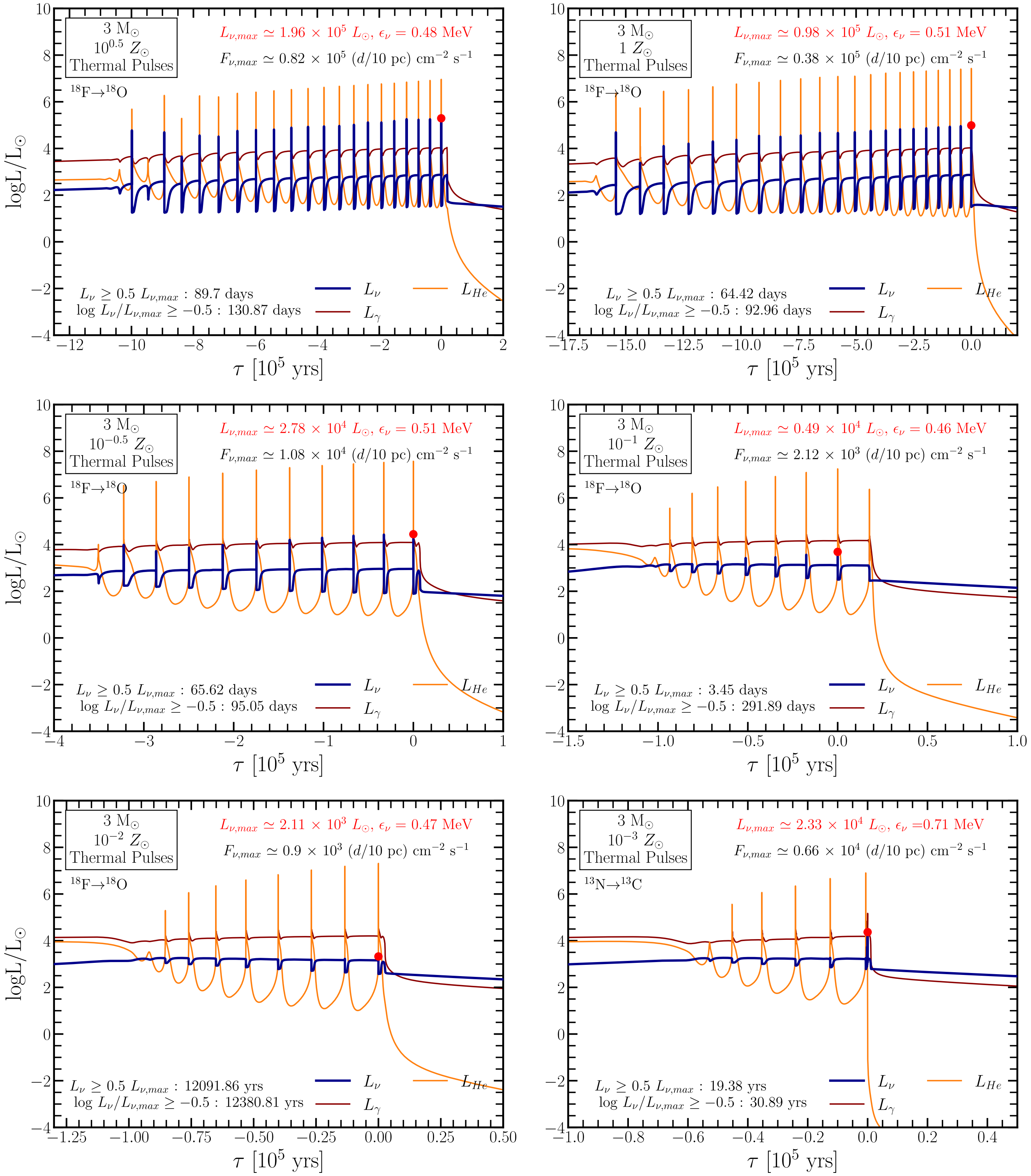

Figure 12. Same format as Figure 11 but for 3 $M_\odot$ models across all six metallicities.

He burning, and ≃10%–30% during the TP-AGB phase. The percentages increase with $M_{\rm ZAMS}$, and with Z for more massive models.

5. High-mass Stars

We present features of the neutrino emission from high-mass models for one metallicity in Section 5.1, and then for all six metallicities in Section 5.2.

5.1. One Metallicity

Tracks from the ZAMS to the onset of CC for the $8\,M_\odot \leqslant M_{\rm ZAMS} \leqslant 150\ M_\odot$ models in a γHRD and νHRD is shown in Figure 14. All tracks evolve at roughly constant L_γ and L_ν during core H burning and He burning as the tracks evolve from the ZAMS to cooler $T_{\rm eff}$. Neutrinos from the CNO cycles and $^{14}{\rm N} \rightarrow\ ^{22}{\rm Ne}$ power L_ν through these phases of evolution. From CHeD onwards, the dominance of L_ν from the

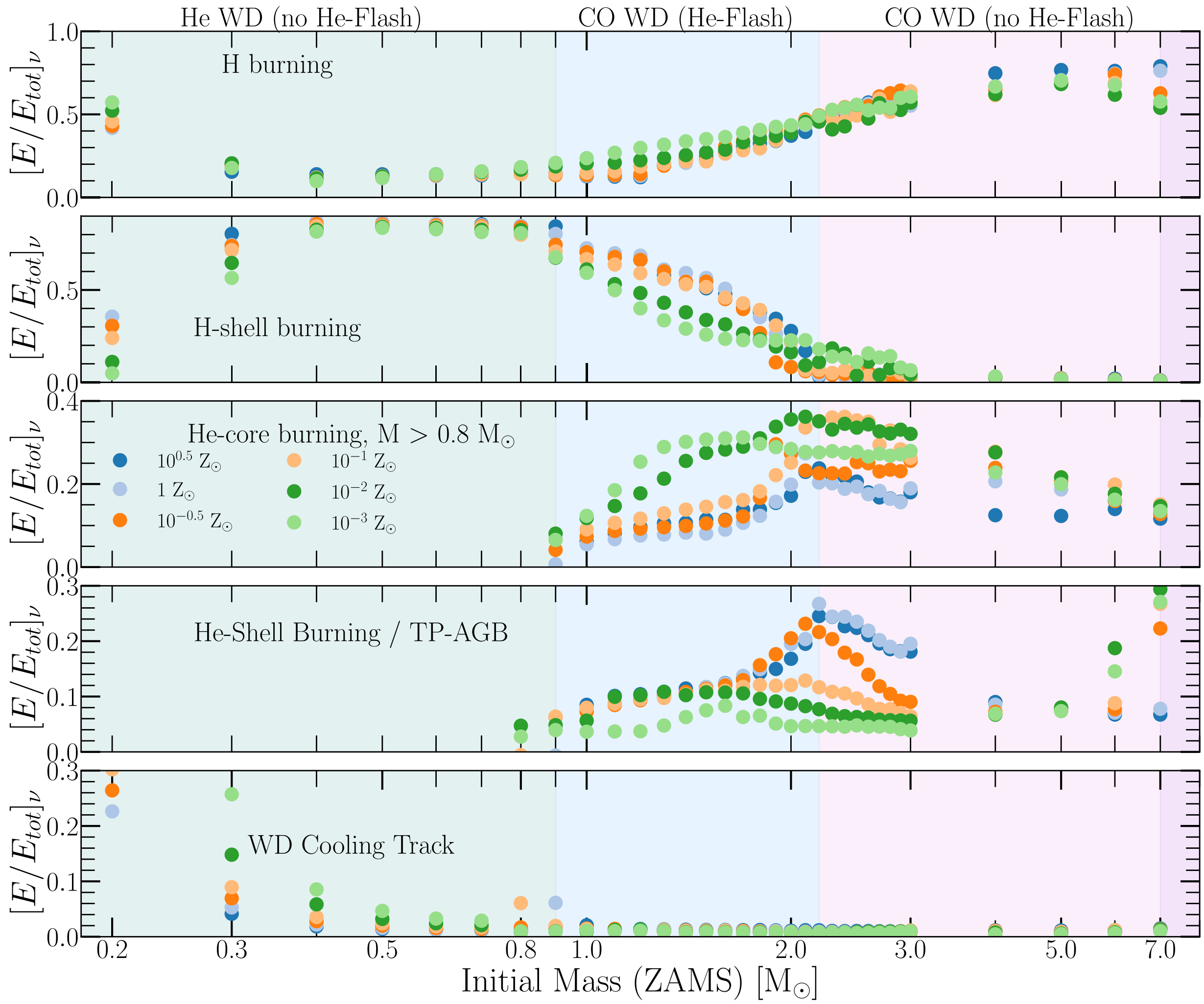

Figure 13. Fraction of E_ν emitted at different phases of evolution for all six metallicities (colored circles). From top to bottom, the panels show $[E/E_{\rm tot}]_\nu$ for core H burning, shell H burning, core He burning prior to any TP-AGB phase, He burning through the TP-AGB phase, and during the WD cooling phase.

core over L_γ from the surface results in a rapid reduction in evolutionary timescales from years to hours to seconds (Fowler & Hoyle 1964; Deinzer & Salpeter 1965; Woosley et al. 2002). This escalating rapidity appears in the νHRD as the nearly vertical curves at approximately constant $T_{\rm eff}$.

For $M_{\rm ZAMS} \lesssim 50\,M_\odot$, the nearly vertical tracks at cooler $T_{\rm eff}$ in the νHRD end their lives as red supergiants (RSGs). The $M_{\rm ZAMS} \gtrsim 50\,M_\odot$ models evolve through the advanced stages at increasingly hotter $T_{\rm eff}$ with thinner H envelopes, until wind-driven mass loss strips the H envelope, creating a Wolf–Rayet model. The nearly vertical tracks at hotter $T_{\rm eff}$ in the νHRD end their lives as a blue supergiants. This transition mass is the Humphrey–Davidson limit in our models (Humphreys & Davidson 1979; Davies et al. 2018; Davies & Beasor 2020; Sabhahit et al. 2021). The conversion of a mass limit to a luminosity limit depends on assumptions. For example, Sabhahit et al. (2021) adopt the luminosity limit as the luminosity above which a massive star model spends <5% of it is lifetime or above the luminosity limit while the model is a yellow/red supergiant. This transition mass is sensitive to the mass and time resolution, mass-loss prescription, and treatment of superadiabatic convection in the outer envelope (Sabhahit et al. 2021).

Another feature in the νHRD of Figure 14 is the radial pulsations in the $35\,M_\odot \lesssim M_{\rm ZAMS} \lesssim 50\,M_\odot$ tracks that develop during He shell or C burning, models with thin H envelopes, and $3.9 \lesssim \log(T_{\rm eff}) \lesssim 4.1$.

C burning sets the entropy for the continued evolution to CC, by proceeding either convectively or radiatively (Murai et al. 1968; Arnett 1972; Lamb et al. 1976). If the energy released by nuclear reactions is slightly larger than pair production neutrino losses, then the net energy produced is transported by convection (e.g., Cristini et al. 2017). Otherwise, the core burns carbon radiatively in balanced power (Woosley et al. 2002; El Eid et al. 2004; Limongi & Chieffi 2018), where the mass-averaged nuclear energy release nearly balances the mass-averaged neutrino losses. For $Z = 1$ $Z_\odot$, tracks for $M_{\rm ZAMS} \leqslant 20$ $M_\odot$ burn carbon convectively (black circles in Figure 14) and tracks with $M_{\rm ZAMS} \geqslant 21\,M_\odot$ burn carbon radiatively (red circles in Figure 14).

The decrease in entropy from thermal neutrino emission that occurs during convective core C burning is missing during radiative core C burning (Weaver & Woosley 1993). For the $M_{\rm ZAMS} \geqslant 21$ $M_\odot$ tracks that undergo radiative C burning, the subsequent burning phases occur at higher entropy, $s \propto T^3/\rho \propto (M/M_\odot)^2$, at higher temperatures, and at lower densities. The larger entropy, in turn, drives shallower and

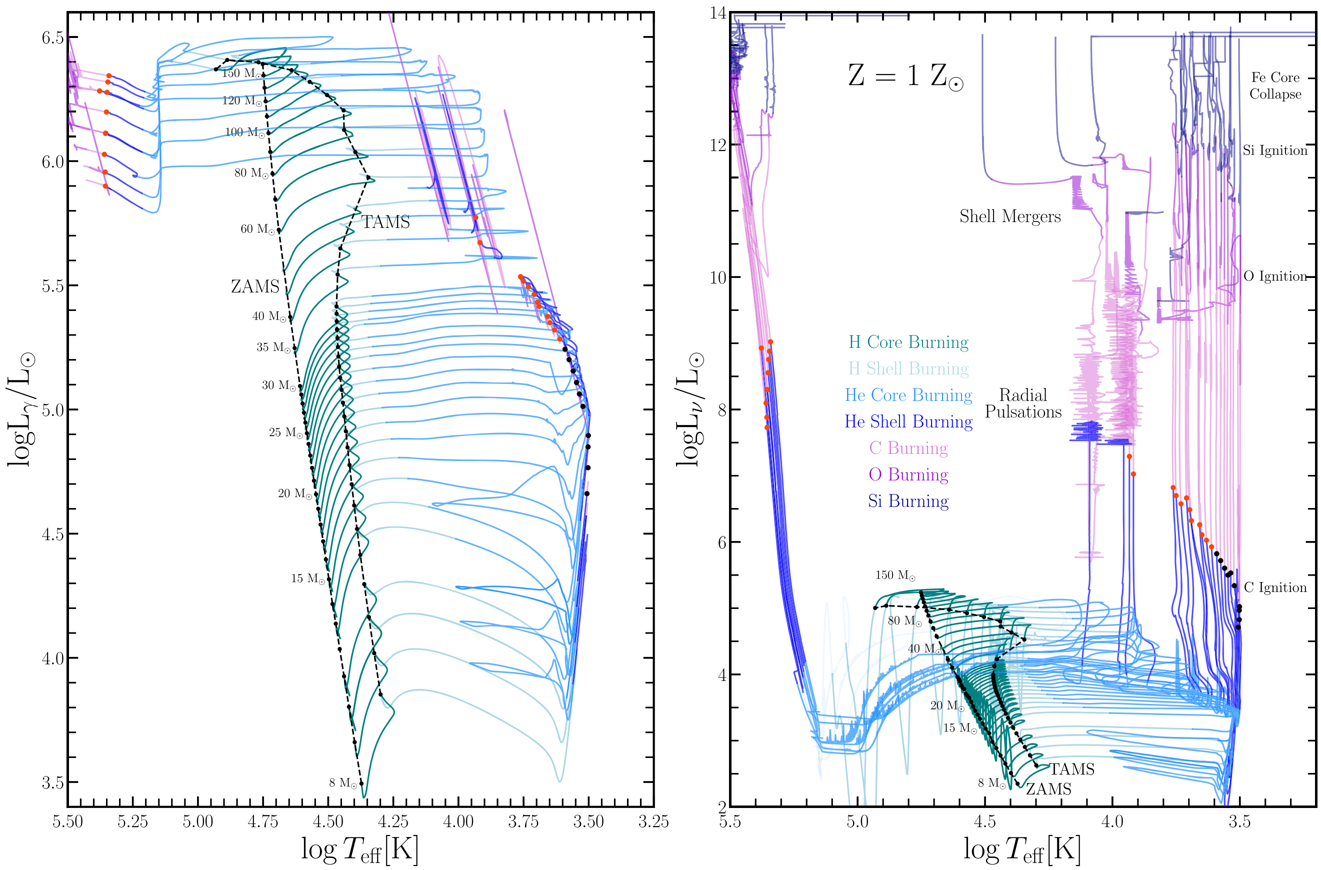

Figure 14. Tracks in a γHRD (left panels) and a νHRD (right panels) for $Z = 1\,Z_\odot$ over $M_{\rm ZAMS} = 8$–$150\,M_\odot$. Tracks are colored by evolutionary phase and labeled. Black circles mark convective core C burning, and red circles mark radiative core C burning. Luminosities are normalized to $L_\odot = 3.828 \times 10^{33}$ erg s^{-1} (Prša et al. 2016).

more extended density gradients, larger effective Chandrasekhar masses at core collapse, smaller compactness parameters, and thus are more challenging to explode as CC events (Woosley & Weaver 1986; Nomoto & Hashimoto 1988; Sukhbold & Woosley 2014; Sukhbold et al. 2016; Limongi & Chieffi 2018; Sukhbold et al. 2018; Sukhbold & Adams 2020; Burrows & Vartanyan 2021). This entropy bifurcation at C burning may seed a bimodal compact object distribution with single stars that undergo convective C burning forming one peak in the compact object initial mass function (neutron stars) and single stars that undergo radiative C burning forming a second peak (black holes; e.g., Timmes et al. 1996; Heger et al. 2003; Zhang et al. 2008; Piro et al. 2017; Sukhbold et al. 2018; Vartanyan et al. 2018; Takahashi et al. 2023).

In the terminal phases Y_e and μ act as guides to the evolution and culminating fate. A dwindling Y_e, catalyzed by electron captures, hastens the core's contraction and amplifies energy depletion through neutrino emissions, thereby altering the core's structural equilibrium. Concurrently, as $Y_e \propto 1/\mu$, an ascending μ signifies a shift toward fusing isotopically heavier nuclei, requiring ever larger core temperatures and densities to maintain hydrostatic equilibrium.

In addition, dynamical large-scale mixing on nuclear burning timescales can occur, as can mergers between the He, C, Ne, O, and Si shells. These shell mergers are sensitive to the mixing scheme adopted and particularly the treatment of convective boundary mixing across shell boundaries (e.g., Ritter et al. 2018; Fields & Couch 2021). An approximate location of these shell mergers is labeled in the νHRD of Figure 14. Strong coupling between nuclear burning and turbulent convection develop during late O burning, which requires 3D simulations to establish the fidelity of the 1D convection approximations (Meakin & Arnett 2007; Couch et al. 2015; Müller et al. 2017; Fields & Couch 2021). As the Fe core approaches its effective Chandrasekhar mass, electron capture and photodisintegration of nuclei drive the onset of CC.

Figure 15 shows the components L_ν for each phase of evolution in the $M_{\rm ZAMS} = 20\,M_\odot$ $Z = 1\,Z_\odot$ model, from shell He burning on the left to CC on the right. After CHeD, the CO core cools and contracts as a convective He-burning shell forms. The first panel on the left shows that the energy budget becomes increasingly dominated by photoneutrino production with $L_\nu \simeq\ 10^5\,L_\odot$.

At $t_{\rm cc} \simeq\ 574$ yr, carbon ignites with $L_\nu \simeq\ 10^6\,L_\odot$ and the energy budget becomes dominated by pair annihilation (second panel). Thermal neutrinos from plasmon decay, bremsstrahlung, and recombination have luminosities several orders of magnitude smaller.

At $t_{\rm cc} \simeq 13.6$ yr, the C shell ignites (third panel), with a sharp increase in $L_{\nu,\rm nuc} = L_{\nu,\beta+} + L_{\nu,\beta^-}\ \simeq\ 10^{6.7}\,L_\odot$. At $t_{\rm cc} \simeq 1.5$ yr, Ne ignites (fourth panel), also with a second sharp increase in $L_{\nu,\beta-}$ and $L_{\nu,\rm nuc}/L_\nu \simeq\ 5\%$. At $t_{\rm cc} \simeq 0.5$ yr (fifth panel), core O ignites. Convection mixes some of the Ne shell into the core, inducing a third spike in $L_{\nu,\beta-}$ and $L_{\nu,\rm nuc}/L_\nu \simeq 15\%$. At $t_{\rm cc} \simeq 11.5$ day (sixth panel), the O–Ne shell ignites, producing a fourth spike with $L_{\nu,\rm nuc} \sim 10^9$ and $L_\nu \sim 10^{11}$, followed shortly by a subdued fifth spike marking the depletion of the Ne shell and the ignition of shell O burning. The common reason for

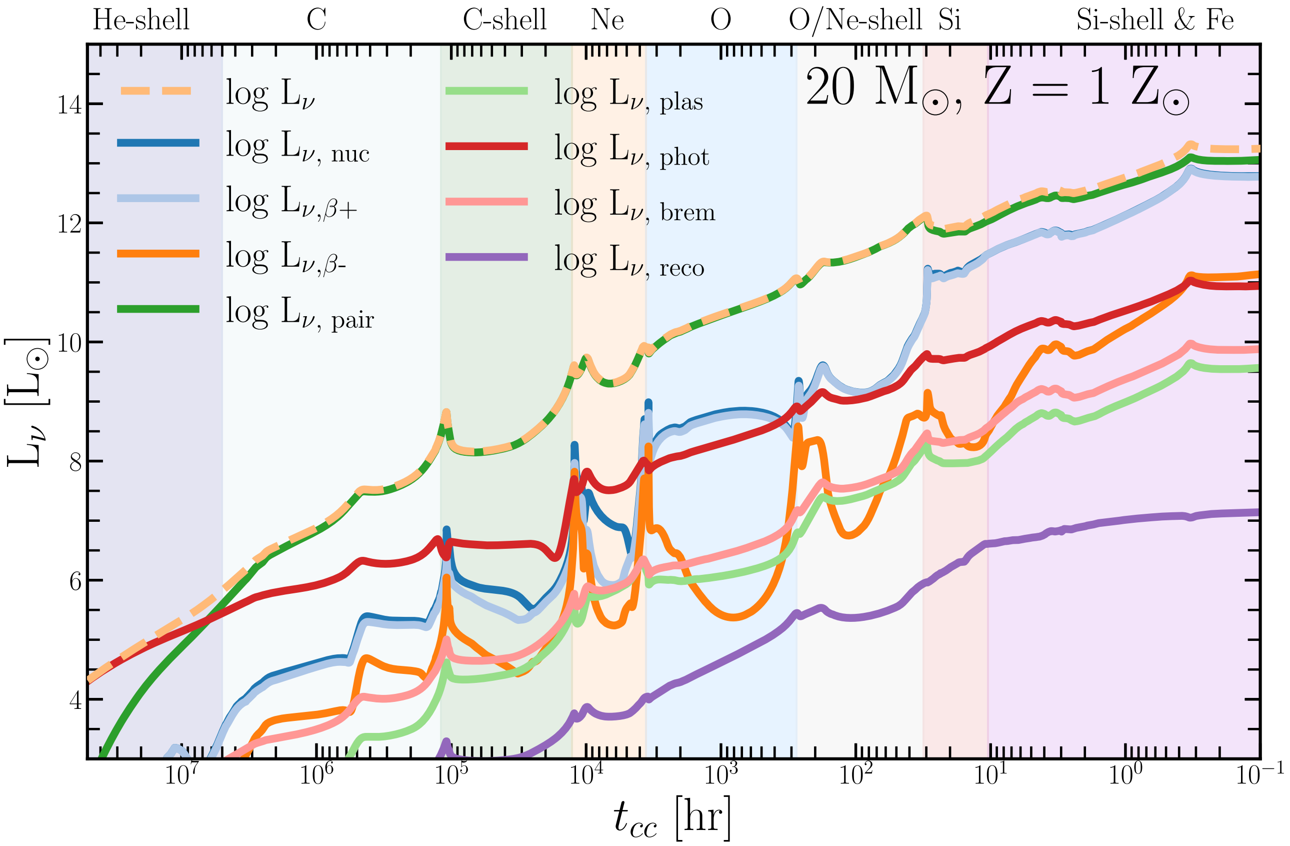

Figure 15. Components of L_ν for each phase of evolution of an $M_{\rm ZAMS} = 20\,M_\odot$, 1 $Z_\odot$ model. The *x*-axis is the time to the onset of CC. Curves show the contributions from nuclear and thermal neutrinos, and are smoothed with a 50 time step moving-average filter. Phases of evolution are shown by the colored regions and labeled above the plot. Boundaries between phases are defined by the ignition of the next fuel source, when the central mass fraction of the next fuel source decreases by 10^{-3}.

these sharp increases (^{22}Ne) is analyzed in detail below. At $t_{\rm cc} \simeq 11.5$ day (seventh panel), the Si core ignites, yielding another phase where $L_{\nu,\rm nuc}/L_\nu \simeq 15\%$. At $t_{\rm cc} \simeq 10$ hr (last panel), the Si shell ignites and ^{56}Fe begins to form through α-capture channels. Shortly after, electron capture and endothermic burning in the Fe core leads to the onset of CC.

Overall, Figure 15 shows thermal processes are the dominant form of neutrino production until Si depletion, when neutrinos from β processes in Fe-group nuclei become a comparable portion of the energy-loss budget until CC. In models that include more Fe-group nuclei in the nuclear network than we do here, neutrinos from β processes surpass thermal neutrino production at the onset of CC (Patton et al. 2017a, 2017b; Farag et al. 2020).

We calculate an approximate pair-neutrino spectrum (Misiaszek et al. 2006; Leung et al. 2020) from

$$\phi_{\rm pair}(\epsilon) = \frac{A}{k_{\rm B}T}\left(\frac{\epsilon}{k_{\rm B}T}\right)^{\gamma} \exp\left(\frac{-a\epsilon}{k_{\rm B}T}\right), \tag{14}$$

where $\phi(\epsilon)$ is the number of emissions with energy ϵ, and the fitting parameters are $\alpha = 3.180657028$, $a = 1.018192299$, and $A = 0.1425776426$. This expression assumes the matter is relativistic and nondegenerate. We also assume all of the neutrinos are produced at the $T_{\rm c}$ of a model, so our estimates serve as upper limits. The average pair-neutrino energy is then

$$\langle\epsilon\rangle_{\rm pair} = \int_0^{1000} \epsilon\phi_{\rm pair}(\epsilon)\,{\rm d}\epsilon, \tag{15}$$

where the integral limits are in MeV. We also cumulatively integrate over the pair-neutrino spectrum to find the lower 10% and upper 90% of neutrino energies of the pair-neutrino spectrum.

We also calculate the average electron neutrino energy ϵ_{ν_e} from β^+ processes and the average electron antineutrino energy $\epsilon_{\bar{\nu}_e}$ from β^- processes as the sum of the energy released per second $\dot{\epsilon}_i$ of each weak reaction i divided by the number luminosity $L_{N,i}$

$$\epsilon_\nu = \sum_{i=1}^{N}(\dot{\epsilon}_i) \bigg/ \sum_{i=1}^{N}(L_{N,i}), \tag{16}$$

where $N = 40$ for the low-mass reaction network and $N = 148$ for the high-mass reaction network of Figure 1.

Figure 16 shows ϵ_{ν_e} and $\epsilon_{\bar{\nu}_e}$ versus $T_{\rm c}$ for different $M_{\rm ZAMS}$ at $Z = 1\,Z_\odot$. During H and He burning, $\epsilon_{\nu_e} \lesssim 1$ MeV, while $\epsilon_{\bar{\nu}_e} \simeq$ 1–1.5 MeV. From C burning to the onset of CC, $\langle\epsilon\rangle_{\rm pair}$ remains well below ϵ_{ν_e} and $\epsilon_{\bar{\nu}_e}$.

During C and Ne burning, β^+ processes are dominated by ^{21,22}Na$\rightarrow$^{21,22}Ne from the Ne–Na cycle and ^{26}Al$\rightarrow$^{26}Mg from the Mg–Al cycle, supplemented by ^{23}Mg$\rightarrow$^{23}Na. These reactions decrease Y_e in the core and produce ν_e with average energies $\epsilon_{\nu_e} \simeq$ 1.6, 1.8, and 1.7 MeV, respectively. During this phase, β^- decays are dominated by ^{28}Si $\leftarrow$^{28}Al, ^{24}Mg $\leftarrow$^{24}Na, and ^{27}Al $\leftarrow$^{27}Mg, producing $\bar{\nu}_e$ with average energies $\epsilon_{\bar{\nu}_e} \simeq$ 1.6, 2.7, and 0.9 MeV, respectively. The total β^- neutrino emission grows from $\simeq$20% of the total β emission during C burning to $\simeq$50% during Ne burning, with ϵ_{ν_e} in the range 1.6–2 MeV, independent of $M_{\rm ZAMS}$.

During Ne and O burning there are windows where the $\epsilon_{\bar{\nu}_e}$ exceeds the $\simeq$1.8 MeV detection threshold to inverse-beta decay of current neutrino detectors (e.g., Simpson et al. 2019;

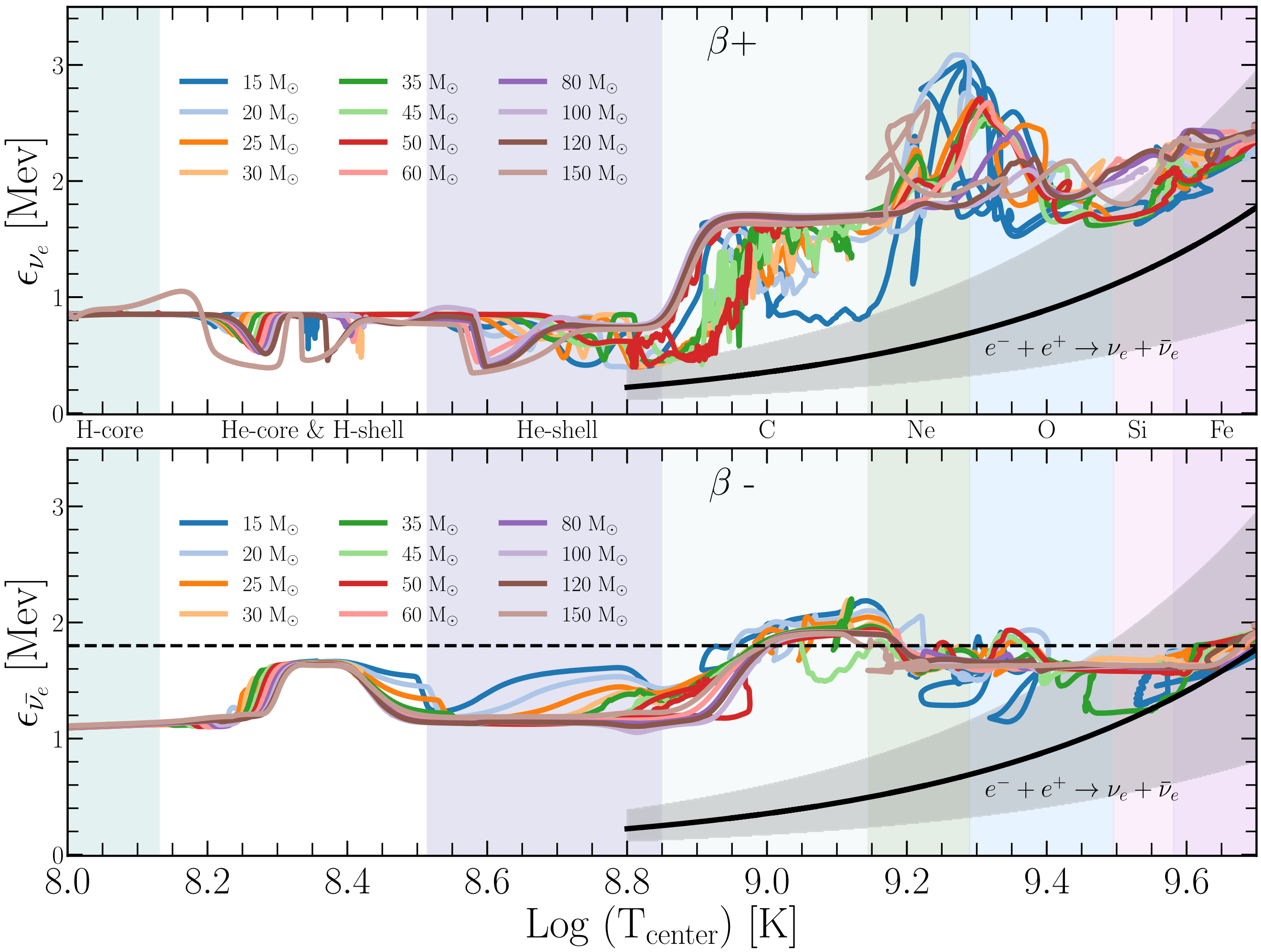

Figure 16. Average electron neutrino energy for beta decays (top), and average electron antineutrino energy for inverse-beta decays (bottom) for the 1 $Z_\odot$ models across a range of $M_{\rm ZAMS}$. Curves are smoothed with a 50 time step moving-average filter. The average pair-neutrino energy is shown by the black curve, with the gray band giving the lower 10% and upper 90% of pair-neutrino energies. Phases of evolution are shown by the colored panels and labeled. The horizontal dashed line shows a representative ≃1.8 MeV detection threshold to inverse-beta decay of current neutrino detectors (e.g., Simpson et al. 2019; Harada et al. 2023). The average electron neutrino and antineutrino energies are approximately independent of $M_{\rm ZAMS}$.

Harada et al. 2023). Table 3 lists the dominant electron antineutrino luminosity sources for the $M_{\rm ZAMS} = 20 M_\odot$ model during the windows where $\bar{\nu}_e$ exceeds current detector thresholds.

The core continues to become more neutron rich during O burning, primarily from $^{31}\mathrm{S} \rightarrow {}^{31}\mathrm{P}$, supplemented by $^{30}\mathrm{P} \rightarrow {}^{30}\mathrm{Si}$ and $^{36}\mathrm{Ar} \rightarrow {}^{36}\mathrm{Cl}$, each producing ν_e with average energies $\epsilon_{\nu_e} \simeq$ 2.2–2.4, 2.4–3.0, and 1.4 MeV, respectively. β processes in the He, C, and Ne shells remain active.

Core and shell Si burning are the last exothermic burning stages and produce the Fe-peak nuclei. Initially $^{31,32}\mathrm{S} \rightarrow {}^{31,32}\mathrm{P}$ and $^{35,36}\mathrm{Ar} \rightarrow {}^{35,36}\mathrm{Cl}$ are the main β-decay channels, but they are quickly replaced by $^{53,54,55}\mathrm{Fe} \rightarrow {}^{53,54,55}\mathrm{Mn}$, $^{51,52,53,54}\mathrm{Mn} \rightarrow {}^{51,52,53,54}\mathrm{Cr}$, $^{51,52,53,54}\mathrm{Mn} \rightarrow {}^{51,52,53,54}\mathrm{Cr}$, $^{55,56,57}\mathrm{Co} \rightarrow {}^{55,56,57}\mathrm{Fe}$, $^{48,49}\mathrm{Cr} \rightarrow {}^{48,49}\mathrm{V}$, and $^{556,57,58,60}\mathrm{Ni} \rightarrow {}^{56,57,58,60}\mathrm{Co}$. Many of the isotopes formed during the final stages undergo β processes that continue to make the core more neutron rich (e.g., Heger et al. 2001; Odrzywolek 2009; Patton et al. 2017b) with $\epsilon_{\nu_e} \simeq$ 2.2 MeV and $\epsilon_{\bar{\nu}_e} \simeq$ 1.8 MeV.

5.2. Six Metallicities

Figure 17 shows the tracks of an $M_{\rm ZAMS} = 20\,M_\odot$ model in a γHRD and a νHRD across all six metallicities. Overall, the low-Z models show the trend of having denser, hotter, and more massive cores with lower envelope opacities, larger surface luminosities, and larger $T_{\rm eff}$ than the high-Z counterparts. The hotter yet more massive H cores extend their MS lifetimes. High-Z models show significantly shorter lifetimes than low-Z models due to their smaller H abundance at the ZAMS. For example, at the ZAMS, $X = 0.75$ for $Z = 10^{-3}\,Z_\odot$ and $X = 0.637$ for $Z = 10^{0.5}\,Z_\odot$. The $Z = 10^{0.5}\,Z_\odot$ model also possesses a significantly smaller H reservoir to burn, due to the large line-driven wind mass-loss prescription ($\dot{M} \propto Z$) that drives the already less massive H-burning region to retreat further inward during the MS evolution, resulting in a significantly shorter MS lifetime than for any other model. Metal-poor tracks have lower envelope opacities and do not evolve to as low a $T_{\rm eff}$ as their metal-rich counterparts. This behavior is especially prominent in the $Z = 10^{-3}\,Z_\odot$ model, the purple curve in Figure 17, which has a much shorter track in the γHRD and is prominently offset from the lower-Z models in the νHRD.

The first and second vertical panels in Figure 18 show the primary source of neutrinos during H burning and He core burning in a 20 $M_\odot$ model is CNO β^+ decays. At CHeD and the onset of shell He burning (third vertical panel), L_ν from β

Table 3
Potential Targets for $\bar{\nu}_e$ Detection

Rate	$L_{\bar{\nu}_e}$ $(L_\odot)$	$L_{N,\bar{\nu}_e}$ (s^{-1})[a]	$\epsilon_{\bar{\nu}_e}$ (MeV)	$t_{\bar{\nu}_e}$[b]	$t_{\bar{\nu}_e}$[b]
`Core Ne`					
$^{28}\mathrm{Si} \leftarrow ^{28}\mathrm{Al}$	$10^{7.78}$	9.0×10^{46}	1.6	7.2 days	11.8 days
$^{24}\mathrm{Mg} \leftarrow ^{24}\mathrm{Na}$	$10^{6.85}$	6.1×10^{45}	2.7	5.3 days	14 days
$^{27}\mathrm{Al} \leftarrow ^{27}\mathrm{Mg}$	$10^{6.61}$	1.0×10^{46}	0.9	5.2 days	7.7 days
`Core O`					
$^{28}\mathrm{Si} \leftarrow ^{28}\mathrm{Al}$	$10^{8.39}$	3.7×10^{47}	1.6	11.7 hr	8.3 hr
$^{24}\mathrm{Mg} \leftarrow ^{24}\mathrm{Na}$	$10^{6.42}$	2.3×10^{45}	2.8	13 days	17.4 days
$^{27}\mathrm{Al} \leftarrow ^{27}\mathrm{Mg}$	$10^{6.01}$	2.6×10^{45}	1.0	6.5 days	9.1 days
`Shell O-Ne`					
$^{28}\mathrm{Si} \leftarrow ^{28}\mathrm{Al}$	$10^{8.58}$	5.7×10^{47}	1.6	13.4 hr	19.3 hr
$^{24}\mathrm{Mg} \leftarrow ^{24}\mathrm{Na}$	$10^{7.56}$	3.1×10^{46}	1.0	20.4 hr	1.24 days
$^{27}\mathrm{Al} \leftarrow ^{27}\mathrm{Mg}$	$10^{7.27}$	4.5×10^{46}	2.8	13.7 hr	19.2 hr

Notes.

[a] Antineutrino number luminosity.

[b] Time period while $L_{\bar{\nu}_e} \geqslant 0.5\ L_{\bar{\nu}_e,\mathrm{max}}$.

[c] Time period while $\log(L_{\bar{\nu}_e}/L_{\bar{\nu}_e,\mathrm{max}}) \geqslant -0.5$. All entries are for the $M_{\mathrm{ZAMS}} = 20\ M_\odot$, $Z = 1\ Z_\odot$ model.

decays decreases while the CO core contracts and heats up. In higher Z models, the dominant source of β neutrinos are from $^{14}\mathrm{N} \rightarrow ^{22}\mathrm{Ne}$ in the growing He-burning shell. In lower Z models where less $^{14}\mathrm{N}$ is present, the dominant source of β neutrinos continues to be from CNO β^+ decays in the active H-burning shell. In all models, thermally excited photoneutrinos in the hot contracting CO core begin to dominate the neutrino emission until temperatures are high enough, $T_c \geqslant 7 \times 10^8$ K, for pair-neutrinos to become the dominant energy-loss mechanisms.

The accumulation of isotopically heavy $^{22}\mathrm{Ne}$ during He burning provides the neutron excess η necessary for β^- decays to occur during advanced burning stages. A fraction of the $^{22}\mathrm{Ne}$ undergoes $^{22}\mathrm{Ne}(\alpha, n)^{25}\mathrm{Mg}$ and to a lesser extent $^{22}\mathrm{Ne}(\alpha,\gamma)^{26}\mathrm{Mg}$. Through CHeD and into C burning, $^{22}\mathrm{Ne}(\alpha, n)^{25}\mathrm{Mg}$ is a neutron source for s-process nucleosynthesis (Peters 1968; Couch et al. 1974; Kappeler et al. 1989; Prantzos et al. 1990; Raiteri et al. 1991b; Gallino et al. 1998; Pignatari et al. 2010; Käppeler et al. 2011; Wiescher et al. 2023).

The fate of neutron-rich $^{25}\mathrm{Mg}$ evolves during C burning (Raiteri et al. 1991a), which is the fusion of two $^{12}\mathrm{C}$ nuclei to form an excited $^{24}\mathrm{Mg}^*$ nucleus that decays in three channels (e.g., Woosley et al. 2002)

$$\begin{aligned} ^{12}\mathrm{C} + ^{12}\mathrm{C} \rightarrow ^{24}\mathrm{Mg}^* \rightarrow\ & ^{20}\mathrm{Ne} + \alpha + \gamma \\ \rightarrow\ & ^{23}\mathrm{Na} + p + \gamma \\ \rightarrow\ & ^{23}\mathrm{Mg} + n + \gamma. \end{aligned} \tag{17}$$

The α- and p-channels occur at similar rates while the n-channel branching ratio is $\sim$1% (Dayras et al. 1977). Uncertainties in the branching ratios and temperature dependent rates can alter the nucleosynthetic yields during C-burning through the Ne–Na or Mg–Al cycles and the amount $^{20}\mathrm{Ne}$ available for Ne melting (Bennett et al. 2012; Pignatari et al. 2013; Zickefoose et al. 2018; Tan et al. 2020; Monpribat et al. 2022).

The fourth vertical panel in Figure 18 shows $^{26}\mathrm{Al} \rightarrow ^{26}\mathrm{Mg}$ (red curve) makes a primary contribution to L_ν from nuclear reactions at all metallicities during C burning. The p-channel powers the Ne–Na cycle, producing a neutrino signal through $^{21,22}\mathrm{Na} \rightarrow ^{21,22}\mathrm{Ne}$ and $^{23}\mathrm{Mg} \rightarrow ^{23}\mathrm{Na}$ β^+ decays. $^{24}\mathrm{Mg}$ is then produced via $^{23}\mathrm{Na}(p,\gamma)^{24}\mathrm{Mg}$, and $^{23}\mathrm{Na}(p,\alpha)^{20}\mathrm{Ne}$ creates stable $^{20}\mathrm{Ne}$—now available for a later stage of Ne melting into $^{24}\mathrm{Mg}$ and $^{28}\mathrm{Si}$. The Mg–Al cycle is weakly powered by the p-channel $^{24}\mathrm{Mg}(p,\gamma)^{25}\mathrm{Al}$ reaction. Instead, the α-channel powers the Mg–Al cycle by providing the He nuclei necessary for $^{22}\mathrm{Ne}(\alpha, n)^{25}\mathrm{Mg}$, which makes the cycle operate. Instead of $^{25}\mathrm{Mg}$ then being consumed by $^{25}\mathrm{Mg}(n,\gamma)^{26}\mathrm{Mg}$, protons from the p-channel power $^{25}\mathrm{Mg}(p,\gamma)^{26}\mathrm{Al}$, which undergoes β^+ decay $^{26}\mathrm{Al} \rightarrow ^{26}\mathrm{Mg}$, dominating the nuclear neutrino production during C burning.

The larger T_c of low-Z models results in a stronger expression of $^{21,22}\mathrm{Na} \rightarrow ^{21,22}\mathrm{Ne}$ during C burning. High-Z models also show a larger β^- luminosity during C burning than their low-Z counterparts. This results from differences in the neutron excess across metallicities. High-Z models enter C burning with a larger $^{22}\mathrm{Ne}$ abundance available for $^{22}\mathrm{Ne}(\alpha, n)^{25}\mathrm{Mg}$, which provides most of the free neutrons for an s-process (Raiteri et al. 1991a; The et al. 2007; Choplin et al. 2018).

Another feature during C burning is that the β^- luminosity declines from $\simeq$50% of the total β neutrino luminosity in the $Z = 10^{0.5}\ Z_\odot$ model to $\simeq$25% in the $Z = 1\ Z_\odot$ model and $\leqslant$10% in lower-Z models. Independent of metallicity, these β^- decays are primarily $^{28}\mathrm{Al} \rightarrow ^{28}\mathrm{Si}$, $^{27}\mathrm{Mg} \rightarrow ^{27}\mathrm{Al}$, and $^{24}\mathrm{Na} \rightarrow ^{24}\mathrm{Mg}$.

Ne melting is characterized by photodisintegration of Ne into α particles, which recapture onto a second Ne nucleus to form $^{16}\mathrm{O}$ and $^{24}\mathrm{Mg}$. The fifth vertical panel in Figure 18 shows that α-capture onto the remaining $^{22}\mathrm{Ne}$ in the core provides a spike in the β^- luminosity, and a neutron source for an s-process. A metallicity dependence on the initial $^{22}\mathrm{Ne}$ content of the core affects the strength of β^- decays at the onset of Ne melting. A significant fraction of the $^{26}\mathrm{Mg}$ also undergoes $^{26}\mathrm{Mg}(\alpha, n)^{30}\mathrm{P}$, which then decays to $^{30}\mathrm{P} \rightarrow ^{30}\mathrm{Si}$.

O burning is the fusion of two $^{16}\mathrm{O}$ nuclei to form an excited state of $^{32}\mathrm{S}^*$, which promptly decays to

$$\begin{aligned} ^{16}\mathrm{O} + ^{16}\mathrm{O} \rightarrow ^{32}\mathrm{S}^* \rightarrow\ & ^{28}\mathrm{Si} + \alpha + \gamma \\ \rightarrow\ & ^{31}\mathrm{P} + p + \gamma \\ \rightarrow\ & ^{31}\mathrm{S} + n + \gamma \\ \rightarrow\ & ^{30}\mathrm{P} + d - \gamma. \end{aligned} \tag{18}$$

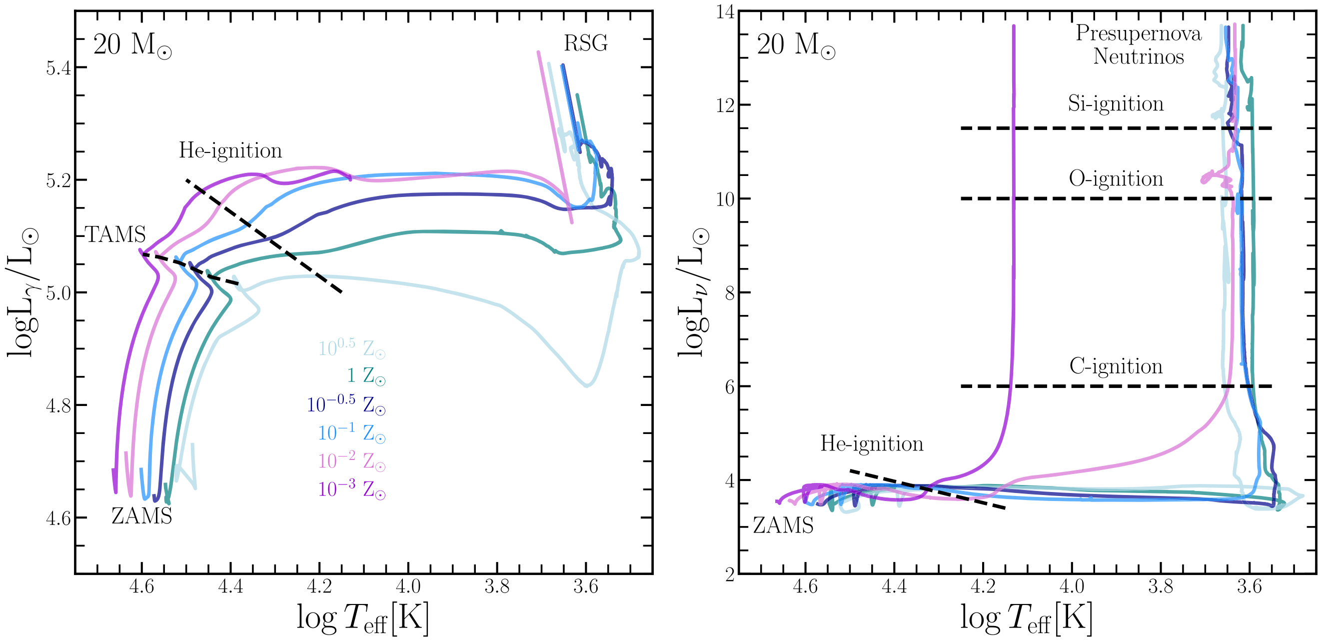

Figure 17. Tracks in a γHRD (left) and νHRD (right) from ZAMS to the onset of CC for the $M_{\rm ZAMS} = 20\,M_\odot$ models across all six metallicities. Approximate locations of evolutionary phases are labeled or marked with a black dashed line. Luminosities are normalized to $L_\odot = 3.828 \times 10^{33}$ erg s^{-1} (Prša et al. 2016).

Branching ratios for the α, p n, and d channels are $\simeq$34%, 56%, 5%, and $\leqslant$5%, respectively, and the products of O burning include ^{28}Si, ^{32,33,34}S, ^{35,36,37}Cl, ^{36,37,38}Ar, ^{39,40,41}K, and ^{40,41,42}Ca (Woosley et al. 2002). The limited extent of neutron-rich isotopes in the high-mass nuclear reaction network of Figure 1 means we do not capture all these isotopes, including ^{35}S and ^{33}P.

The sixth vertical panel in Figure 18 shows that $^{31}\mathrm{S} \rightarrow {}^{31}\mathrm{P}$ makes a primary contribution to L_ν from nuclear reactions at all metallicities during O burning. The accumulation of ^{36}Ar leads to a growing neutrino signal from $^{36}\mathrm{Ar} \rightarrow {}^{36}\mathrm{Cl}$. After core O depletion, shell Ne melting occurs before O-shell burning. The α-captures onto the remaining ^{22}Ne nuclei in the shell provides a second spike in the β^- luminosity in Figure 18.

From Si burning (Si-α) until CC, the seventh and eighth vertical panel in Figure 18, there are little differences in the relative strength of individual β decays. At this stage of evolution, the expression of Fe-group β decays is metallicity independent, and β^- decays remain subdominant until $t_{cc} \lesssim 10^{-1}$ hr (Patton et al. 2017a, 2017b; Kato et al. 2017, 2020a; Kosmas et al. 2022).

In Figure 19 the average neutrino and antineutrino energies are, to first order, similar across metallicities for β^+ and β^- decays in a 20 $M_\odot$ model. The largest differences in antineutrino energies occur during C-shell and Ne-core burning, when the neutron excess provided by ^{22}Ne is most important. Metal-poor tracks possess lower L_{β^-}, but higher overall average antineutrino energy, since the signal is increasingly dominated by $^{24}\mathrm{Mg} \leftarrow {}^{24}\mathrm{Na}$ as opposed to $^{28}\mathrm{Si} \leftarrow {}^{28}\mathrm{Al}$. Windows where $\bar{\nu}_e$ exceeds current detector thresholds are listed in Table 3 for the $Z = 1\,Z_\odot$ model.

Figure 20 shows the fraction of the total neutrino energy produced during different phases of evolution in the mass–metallicity plane. The spread reflects the different fates experienced by stellar models of differing mass–metallicity. Larger spreads occur for the high-mass models where wind-driven mass loss and shell-core mergers contribute.

Across metallicities in Figure 20, the chief nuclear neutrino production in high-mass models come from the CNO cycle during H burning, accounting for $\simeq$40%–90% of the total neutrino emission with a trend toward larger fractions with increasing $M_{\rm ZAMS}$. Typical fractions for He burning are $\lesssim$8%, with an exception for some very massive models that produce $\simeq$10%–20% from recurrent mixing of the shell H into the He core before CHeD. Typical fractions for C burning and O burning are $\simeq$5%–20% and $\simeq$5%–30%, respectively, with a negative trend toward higher masses. From core-Si ignition to CC, $\simeq$ 2%–10% of the total neutrino emission occurs with a negative trend toward increasing masses. Overall, most neutrinos are produced during H and He burning from β^+ decays, especially in the most massive models.

6. Integrated Stellar Photon and Neutrino Emission

We explore the time-integrated photon and neutrino emission of a simple stellar population model. We assume a burst cluster population where all models are born at the same time and evolve together.

$$N_0 = \frac{1}{M_\odot}\int_{M_{\rm min\,0}}^{M_{\rm max}} \frac{dN}{dm} M_* \, dm, \tag{19}$$

$$\Phi(t) = \frac{1}{N_0}\int_{M_{\rm min}}^{M_{\rm max}} \frac{dN}{dm} \phi(m, t)\, dm, \tag{20}$$

We adopt the normalized broken power law initial mass function (IMF) from Kroupa (2001) for the number of stars per unit mass dN/dm. We integrate over the IMF in Equation (19) to solve for a normalization coefficient such that a cluster of mean mass 1 $M_\odot$ is formed in the burst of star formation. The minimum mass $M_{\rm min\,0} = 0.01\,M_\odot$ and the maximum mass $M_{\rm max} = 150\,M_\odot$ of the IMF set the integration limits for the 1 $M_\odot$ stellar cluster. We then solve Equation (20) for $\Phi(t)$, the resultant integrated quantity, where $\phi(t)$ is the quantity we source along an isochrone. The minimum mass

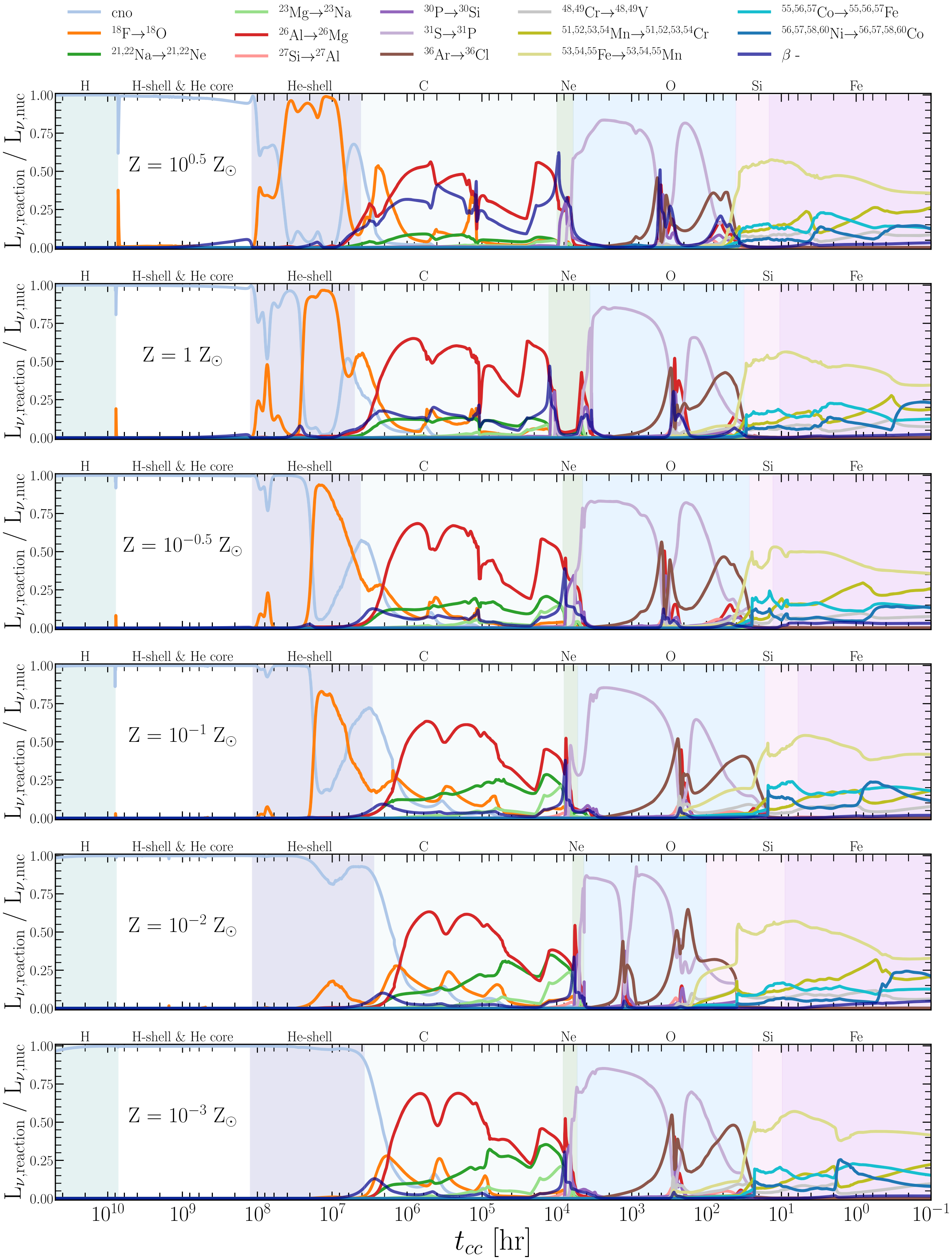

Figure 18. Components of L_ν from nuclear reactions over the lifetime of an $M_{\mathrm{ZAMS}} = 20\ M_\odot$ model for all six metallicities. The *x*-axis is the time to the onset of CC. Evolutionary phases are shown by the colored regions and labeled. Curves show the largest contributions by the burning processes and weak reactions listed in the legend.

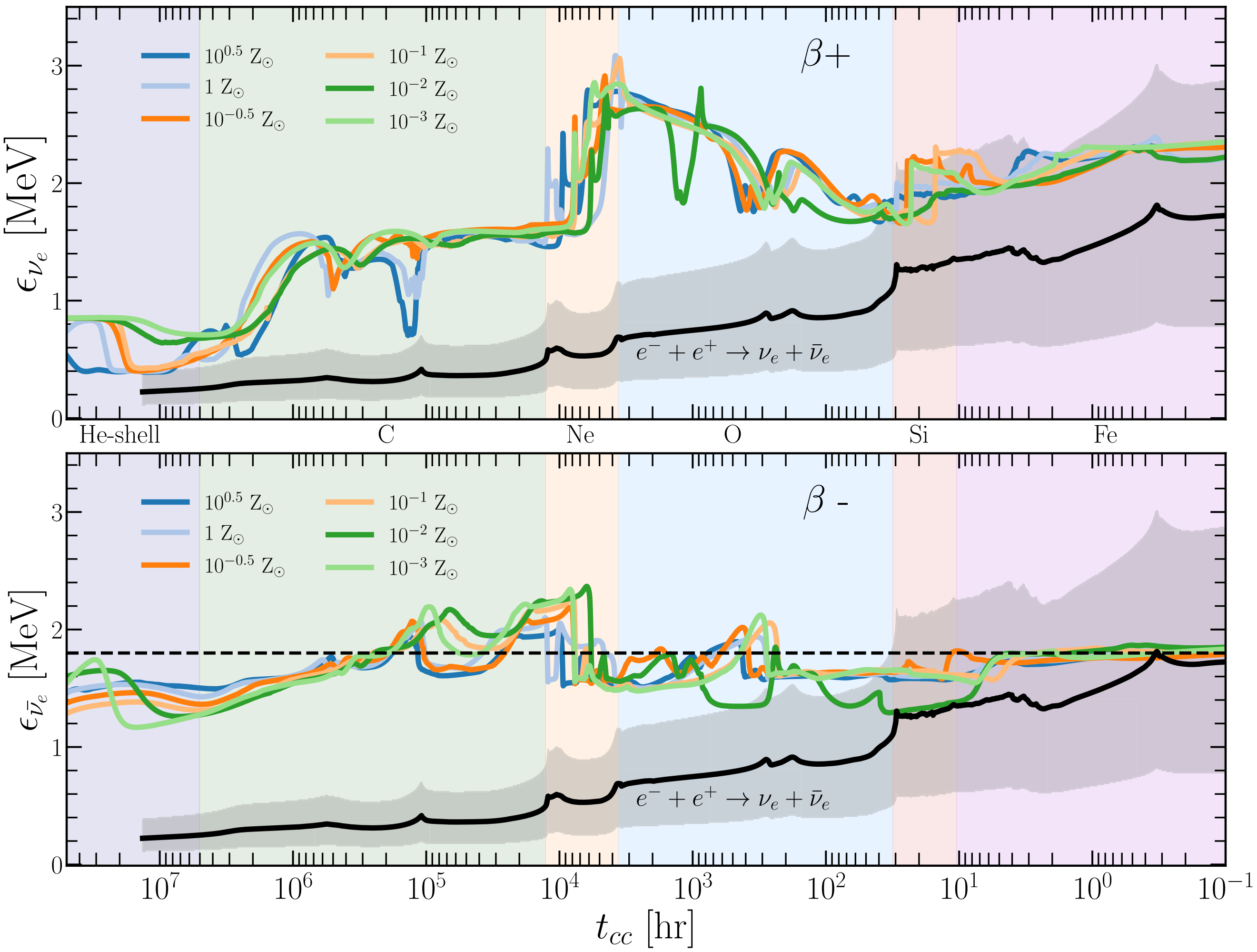

Figure 19. Average electron neutrino energy for beta decays (top), and average electron antineutrino energy for inverse-beta decays (bottom) for the $M_{\rm ZAMS} = 20\, M_\odot$ models across all six metallicities. Curves are smoothed with a 50 time step moving-average filter. The average pair-neutrino energy is shown by the black curve, with the gray band giving the lower 10% and upper 90% pair-neutrino energies. Phases of evolution are shown by the colored panels and labeled. The horizontal dashed line shows a representative ≃1.8 MeV detection threshold to inverse-beta decay of current neutrino detectors (e.g., Simpson et al. 2019; Harada et al. 2023). The average electron neutrino and antineutrino energies are to first order independent of Z.

$M_{\rm min\,0} = 0.2\, M_\odot$ and the maximum mass $M_{\rm max} = 150\, M_\odot$ of the mass–metallicity plane set the integration limits.

Figure 21 shows L_γ and L_ν light curves for each population synthesis model, sampled at 600,000 points in log(Age) for each metallicity. We overlay a quadratic power law for each population synthesis model to provide a convenient fitting formula for L_γ and L_ν as a function of the stellar cluster age and mass

$$\log\left(\frac{L}{L_\odot}\right) = \left[a \log\left(\frac{\rm Age}{\rm yr}\right)^2 - b \log\left(\frac{\rm Age}{\rm yr}\right) + c\right] + \log\left(\frac{M}{M_\odot}\right) \tag{21}$$

where the fit coefficients (a, b, c) are listed in Table 4.

Figure 22 shows the cluster L_γ and L_ν light curves and their ratio of L_γ/L_ν. Both L_γ and L_ν are slightly larger in low-Z models until $\sim 10^{10.5}$ Gyr when low-Z models are depleted of most H-burning and He-burning stellar tracks, and L_γ and L_ν become comparable across all metallicities (except for $Z = 10^{0.5}$ $Z_\odot$). Low-Z stellar population fits show an overall larger L_γ/L_ν than high-Z fits until $\sim 10^{10.5}$ Gyr, when the population synthesis models are dominated by very low-mass models $M_{\rm ZAMS} \leqslant 0.8\, M_\odot$.

Figure 23 shows the $\epsilon_{\bar{\nu}_e}$, $\epsilon_{\bar{\nu}_e}$, $B - V$ color, $V - K$ color, and the light to mass ratio in the V band versus cluster age for all six metallicities. Photon and neutrino emission at early times $\simeq 10^7$ yr is indicative of high-mass model emissions. By $\simeq 10^8$ yr, all high-mass models have reached their final fate, leaving only low-mass models in the stellar population. Most of a star's life is spent during H and He burning in which neutrino emission is dominated by β processes; therefore, it is reasonable to approximate the average neutrino energy of a simple stellar population by β processes alone.

The top panel in Figure 23 shows that the average neutrino energy from a simple stellar population model ranges 0.5–1 MeV. Average neutrino energies show a slight metallicity trend, with low-Z models producing up to 0.5 MeV larger signal than high-Z models in the age range 10^7–$10^{9.5}$ yr, then decreasing to ≃0.5 MeV at $10^{10.5}$ yr. The second panel shows the average antineutrino energy ranges 0.6–1.8 MeV. The antineutrino emission at early times, $\simeq 10^7$ yr, is dominated by high-mass models reaching up to ∼1.8 MeV. By $\simeq 10^8$ yr, the antineutrino energy has reduced to ≃0.6 MeV and remains roughly constant until $10^{10.5}$ yr.

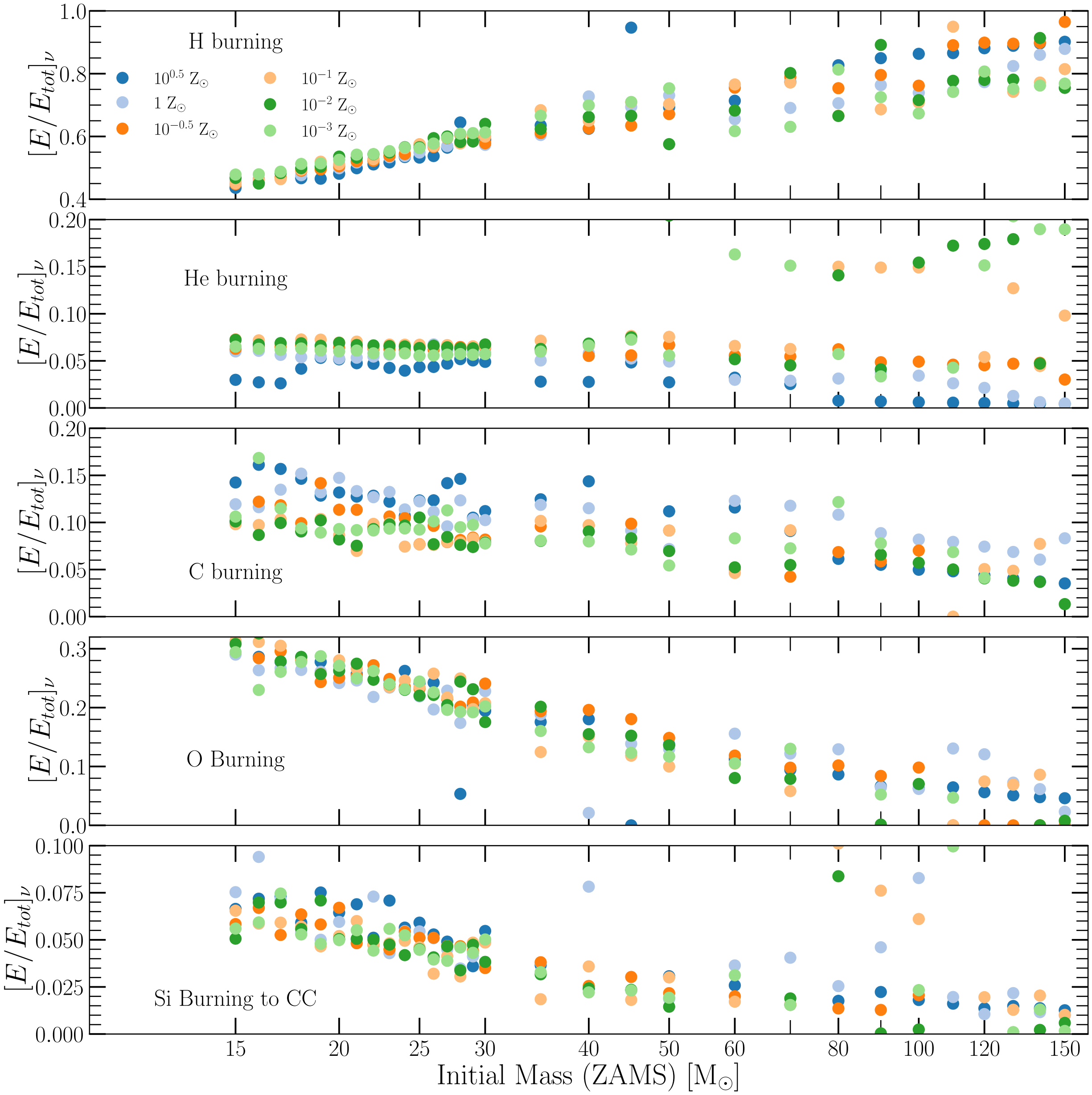

Figure 20. Fraction of E_ν emitted at different phases of evolution for all six metallicities (colored circles). From top to bottom, the panels show $[E/E_{\rm tot}]_\nu$ for H burning, He burning, C burning, O burning and Si burning to the onset of CC.

The third and fourth panels in Figure 23 shows the Johnson–Cousins $B - V$ and $V - K$ colors, respectively, calculated using the tabulations from Lejeune et al. (1998). At early times, $\simeq 10^7$ yr, there is a slight excess in $B - V$ and a relatively large jump in $V - K$ from the high-Z population models, roughly at the onset of the RSG phase in the high-mass models (Choi et al. 2016). The bump in $V - K$ is suppressed in the lowest-metallicity models, which do not evolve toward the RSG branch and instead remain relatively blue, with RSG color spectra similar to the MS. At late times, $\gtrsim 10^9$ yr when the population contains only low-mass stars, the $B - V$ and $V - K$ colors show an overall reddening in high-Z stellar populations.

The V-band light to mass ratio in the bottom panel of Figure 23 shows a weak but distinct metallicity trend. At early times, L_V/M is larger in the lower-metallicity populations. This is due to the increased L_γ in low-Z models. At late times, the trend is inverted with larger L_V/M in the high-Z population models. This is due to the longer MS lifetimes in the high-Z population models.

7. Summary

We explored the evolution of stellar neutrino emission with 420 models spanning the initial mass $0.2\,M_\odot \leqslant M_{\rm ZAMS} \leqslant 150\,M_\odot$ and initial metallicity $-3 \leqslant \log(Z/Z_\odot) \leqslant 0.5$ plane. We found lower-metallicity models are more compact, hotter, and produce larger L_ν with two exceptions. At He-core ignition on the RGB and He-shell burning on the AGB, the birth metallicity determines the amount of ^{14}N available for the nitrogen flash ^{14}N(α,γ)^{18}F($,e^+\nu_e$)^{18}O. In high-mass models, the birth metallicity determines the amount of ^{14}N and therefore ^{22}Ne available for ^{22}Ne(α, n)^{25}Mg, providing a neutron excess to power antineutrino emission during C, Ne, and O burning. Overall, across the mass–metallicity plane we identify the

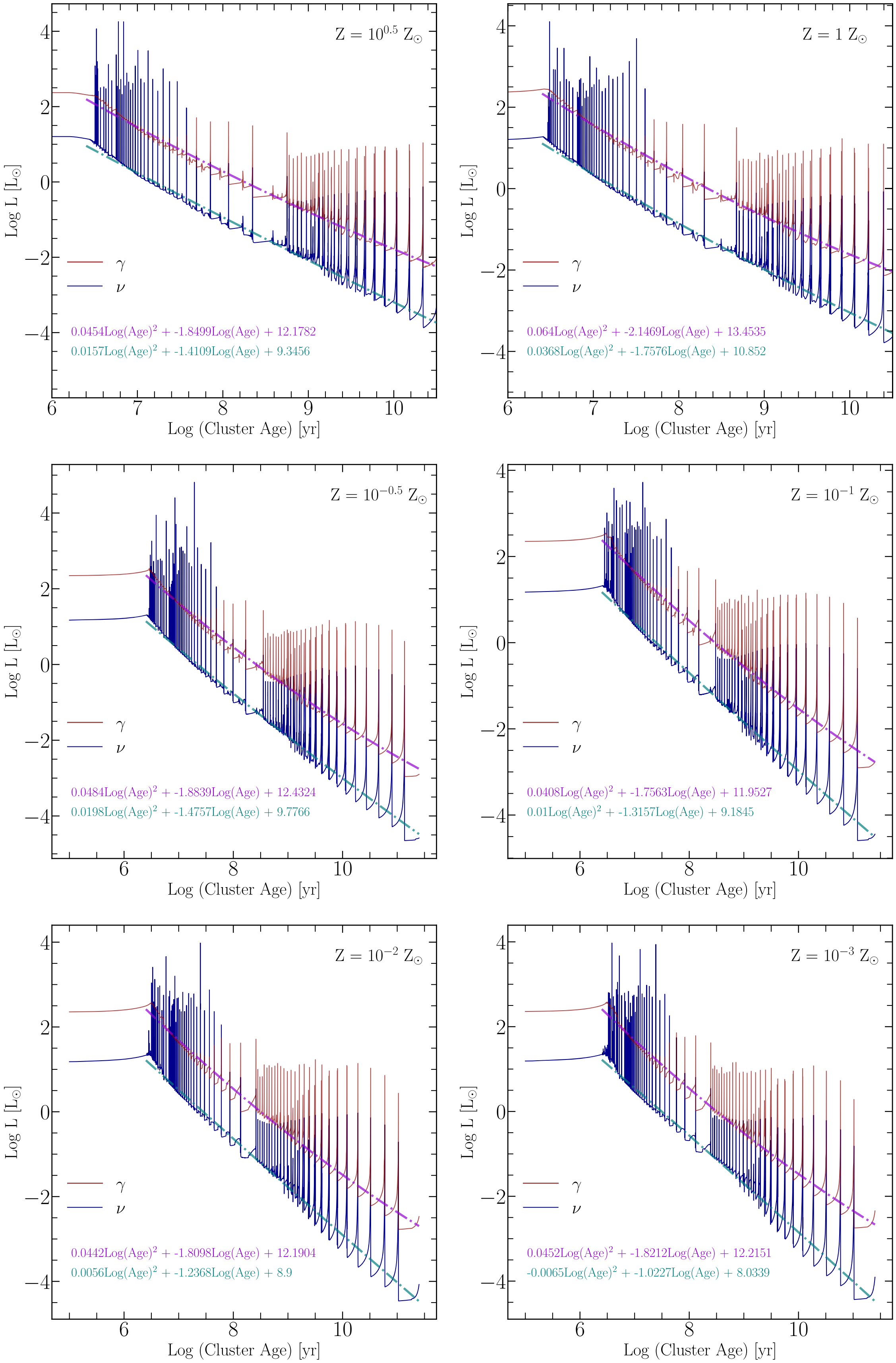

Figure 21. Cluster L_γ and L_ν light curves from the evolution models for all six metallicities. Overlayed are quadratic fitting functions with the coefficients for each metallicity listed (see Equation (21)).

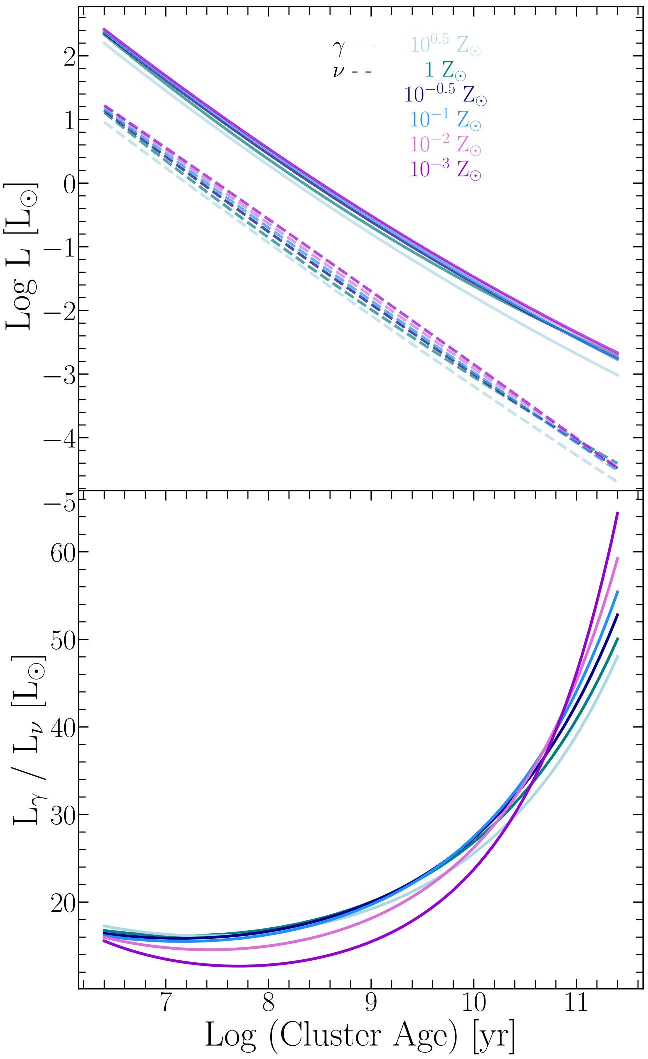

Figure 22. Cluster L_γ and L_ν light curves (top) and the ratio L_γ/L_ν (bottom) using Equation (21) with $M = 1\ M_\odot$ for all six metallicities.

Table 4
Fit Coefficients of Equation (21)

	a	*b*	*c*
For $Z = 10^{0.5}\ Z_\odot$			
L_γ	0.0454	1.8499	12.1782
L_ν	0.0157	1.4109	9.3456
For $Z = 10^{0.0}\ Z_\odot$			
L_γ	0.0640	2.1469	13.4535
L_ν	0.0368	1.7576	10.8520
For $Z = 10^{-0.5}\ Z_\odot$			
L_γ	0.0484	1.8839	12.4324
L_ν	0.0198	1.4757	9.7766
For $Z = 10^{-1.0}\ Z_\odot$			
L_γ	0.0408	1.7563	11.9527
L_ν	0.0100	1.3157	9.1845
For $Z = 10^{-2.0}\ Z_\odot$			
L_γ	0.0442	1.8098	12.1904
L_ν	0.0056	1.2368	8.9000
For $Z = 10^{-3.0}\ Z_\odot$			
L_γ	0.0452	1.8212	12.2151
L_ν	−0.0065	1.0227	8.0339

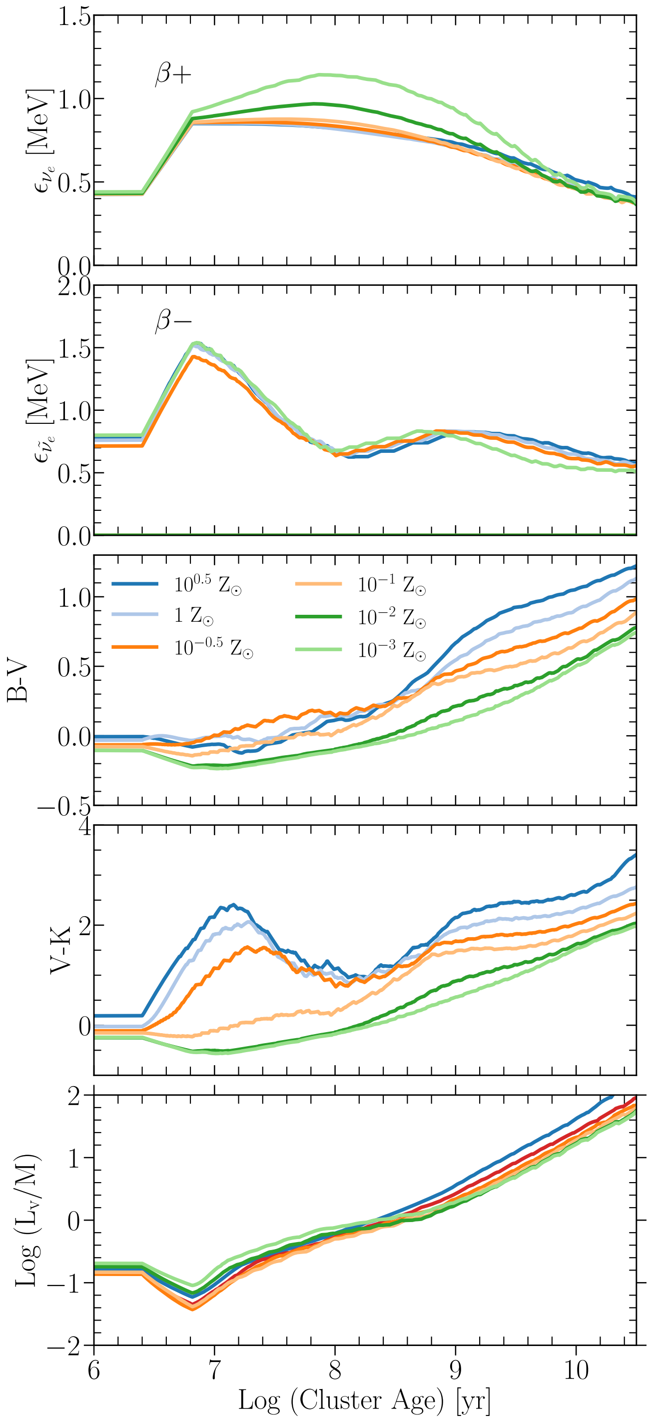

Figure 23. Average electron neutrino energies for beta decay processes (top panel), average electron antineutrino energies for inverse-beta decay processes (second panel), Johnson–Cousins $B - V$ and $V - K$ colors (third and fourth panels), and neutrino light to mass ratio for a simple stellar population (bottom panel) for all six metallicities.

sequence $Z_{\rm CNO} \rightarrow {}^{14}{\rm N} \rightarrow {}^{22}{\rm Ne} \rightarrow {}^{25}{\rm Mg} \rightarrow {}^{26}{\rm Al} \rightarrow {}^{26}{\rm Mg} \rightarrow {}^{30}{\rm P} \rightarrow {}^{30}{\rm Si}$ as making primary contributions to L_ν at different phases of evolution.

Simple stellar populations with lower birth metallicities have higher overall L_ν than their metal-rich counterparts. We find that most neutrinos from simple stellar populations are emitted in the form of electron neutrinos through β^+ decays, with average energies in the range 0.5–1.2 MeV. Lastly, we find that metal-poor stellar populations produce larger average β^+ neutrino energies (up to 0.5 MeV), though this trend is much weaker, if resolved, for β^- neutrino emission.

We close this article by pointing out that there are many potential sensitivities that we have not investigated. Examples include choosing different convective mixing prescriptions, mass-loss algorithms, and nuclear reaction rate probability distribution functions (especially ^{12}C(α,γ)^{16}O and triple-α). We also neglected rotation, associated magnetic fields, and binary interactions. Future uncertainty quantification studies could also explore potential couplings between simultaneous variations in uncertain parameters. We caution that these uncertainties, or missing physics, could alter the neutrino emission properties of our models.

Acknowledgments

We thank Thomas Steindal for his helpful discussions. We acknowledge using ChatGPT (OpenAI 2023) to help polish the language of one paragraph (Vishniac 2023). This research is supported by the National Science Foundation (NSF) under grant No. 2154339 entitled “Neutrino Emission From Stars.” This research made extensive use of the SAO/NASA Astrophysics Data System (ADS).

Facility: ASU:RC

Software: `MESA` (Paxton et al. 2011, 2013, 2015, 2018, 2019; Jermyn et al. 2023, https://docs.mesastar.org), `MESASDK` 20190830 (Townsend 2019a, 2019b), `matplotlib` (Hunter 2007), and `NumPy` (van der Walt et al. 2011), `ChatGPT` (OpenAI 2023).

ORCID iDs

Ebraheem Farag https://orcid.org/0000-0002-5794-4286
F. X. Timmes https://orcid.org/0000-0002-0474-159X
Morgan T. Chidester https://orcid.org/0000-0002-5107-8639
Samalka Anandagoda https://orcid.org/0000-0002-5490-2689
Dieter H. Hartmann https://orcid.org/0000-0002-8028-0991

References

Abe, K., Haga, Y., Hayato, Y., et al. 2016, APh, 81, 39
Abe, S., Asami, S., Eizuka, M., et al. 2023, PhRvL, 130, 051801
Acciarri, R., Acero, M. A., Adamowski, M., et al. 2016, arXiv:1601.02984
Ackermann, M., Bustamante, M., Lu, L., et al. 2022, JHEAp, 36, 55
Ahmad, Q. R., Allen, R. C., Andersen, T. C., et al. 2002, PhRvL, 89, 011301
Al Kharusi, S., BenZvi, S. Y., Bobowski, J. S., et al. 2021, NJPh, 23, 031201
Alastuey, A., & Jancovici, B. 1978, ApJ, 226, 1034
Alekseev, E. N., Alekseeva, L. N., Volchenko, V. I., & Krivosheina, I. V. 1987, JETPL, 45, 589
Allega, A., Anderson, M. R., Andringa, S., et al. 2023, PhRvL, 130, 091801
Almeida-Fernandes, F., Placco, V. M., Rocha-Pinto, H. J., et al. 2023, MNRAS, 523, 2934
Althaus, L. G., & Córsico, A. H. 2022, A&A, 663, A167
Alves, D. R., & Sarajedini, A. 1999, ApJ, 511, 225
An, F. P., Bai, W. D., Balantekin, A. B., et al. 2023, PhRvL, 130, 161802
Anandagoda, S., Hartmann, D. H., Ajello, M., & Desai, A. 2020, RNAAS, 4, 4
Anandagoda, S., Hartmann, D. H., Fryer, C. L., et al. 2023, ApJ, 950, 29
Ando, S., & Sato, K. 2004, NJPh, 6, 170
Angulo, C., Arnould, M., Rayet, M., et al. 1999, NuPhA, 656, 3
Arnett, W. D. 1972, ApJ, 176, 699
Arnould, M., Goriely, S., & Jorissen, A. 1999, A&A, 347, 572
Asplund, M., Grevesse, N., Sauval, A. J., & Scott, P. 2009, ARA&A, 47, 481
Bahcall, J. N. 1989, Neutrino Astrophysics (Cambridge: Cambridge Univ. Press.)
Bauer, E. B. 2023, ApJ, 950, 115
Bauer, E. B., Schwab, J., Bildsten, L., & Cheng, S. 2020, ApJ, 902, 93
Beacom, J. F. 2010, ARNPS, 60, 439
Beacom, J. F., & Vogel, P. 1999, PhRvD, 60, 033007
Becker, S. A., & Iben, I., Jr. 1979, ApJ, 232, 831
Becker, S. A., & Iben, I., Jr. 1980, ApJ, 237, 111
Bennett, M. E., Hirschi, R., Pignatari, M., et al. 2012, MNRAS, 420, 3047
Bildsten, L., Paxton, B., Moore, K., & Macias, P. J. 2012, ApJL, 744, L6
Bionta, R. M., Blewitt, G., Bratton, C. B., et al. 1987, PhRvL, 58, 1494
Bischoff-Kim, A., & Montgomery, M. H. 2018, AJ, 155, 187
Bisnovatyi-Kogan, G. S., & Seidov, Z. F. 1984, NYASA, 422, 319
Blöcker, T. 2001, Ap&SS, 275, 1
Bloecker, T., & Schoenberner, D. 1997, A&A, 324, 991
Blouin, S., Shaffer, N. R., Saumon, D., & Starrett, C. E. 2020, ApJ, 899, 46
Boeltzig, A., deBoer, R. J., Chen, Y., et al. 2022, PhRvC, 106, 045801
Borexino Collaboration, Agostini, M., Altenmüller, K., et al. 2018, Natur, 562, 505
Borexino Collaboration, Agostini, M., Altenmüller, K., et al. 2020, Natur, 587, 577
Borexino Collaboration, Bellini, G., Benziger, J., et al. 2014, Natur, 512, 383
Bravo, E., Domínguez, I., Badenes, C., Piersanti, L., & Straniero, O. 2010, ApJL, 711, L66
Brocato, E., Castellani, V., degl'Innocenti, S., Fiorentini, G., & Raimondo, G. 1998, A&A, 333, 910
Burrows, A., & Vartanyan, D. 2021, Natur, 589, 29
Campante, T. L., Schofield, M., Kuszlewicz, J. S., et al. 2016, ApJ, 830, 138
Capozzi, F., & Raffelt, G. 2020, PhRvD, 102, 083007
Casamiquela, L., Soubiran, C., Jofré, P., et al. 2021, A&A, 652, A25
Cassisi, S., Potekhin, A. Y., Pietrinferni, A., Catelan, M., & Salaris, M. 2007, ApJ, 661, 1094
Cassisi, S., & Salaris, M. 2013, Old Stellar Populations: How to Study the Fossil Record of Galaxy Formation (Weinheim: Wiley-VCH)
Chidester, M. T., Farag, E., & Timmes, F. X. 2022, ApJ, 935, 21
Chidester, M. T., Timmes, F. X., Schwab, J., et al. 2021, ApJ, 910, 24
Choi, J., Dotter, A., Conroy, C., et al. 2016, ApJ, 823, 102
Choplin, A., Hirschi, R., Meynet, G., et al. 2018, A&A, 618, A133
Chugunov, A. I., Dewitt, H. E., & Yakovlev, D. G. 2007, PhRvD, 76, 025028
Clayton, G. C., & De Marco, O. 1997, AJ, 114, 2679
Córsico, A. H., Althaus, L. G., Miller Bertolami, M. M., & Kepler, S. O. 2019, A&ARv, 27, 7
Couch, R. G., Schmiedekamp, A. B., & Arnett, W. D. 1974, ApJ, 190, 95
Couch, S. M., Chatzopoulos, E., Arnett, W. D., & Timmes, F. X. 2015, ApJL, 808, L21
Cristini, A., Meakin, C., Hirschi, R., et al. 2017, MNRAS, 471, 279
Cyburt, R. H., Amthor, A. M., Ferguson, R., et al. 2010, ApJS, 189, 240
Da Costa, G. S., & Armandroff, T. E. 1990, AJ, 100, 162
Davies, B., & Beasor, E. R. 2020, MNRAS, 493, 468
Davies, B., Crowther, P. A., & Beasor, E. R. 2018, MNRAS, 478, 3138
Dayras, R., Switkowski, Z. E., & Woosley, S. E. 1977, NuPhA, 279, 70
De Gerónimo, F. C., Miller Bertolami, M. M., Plaza, F., & Catelan, M. 2022, A&A, 659, A150
deBoer, R. J., Görres, J., Wiescher, M., et al. 2017, RvMP, 89, 035007
Deinzer, W., & Salpeter, E. E. 1965, ApJ, 142, 813
Demarque, P. 1960, ApJ, 132, 366
Demarque, P. 1967, ApJ, 149, 117
Denissenkov, P. A., Truran, J. W., Herwig, F., et al. 2015, MNRAS, 447, 2696
Dewitt, H. E., Graboske, H. C., & Cooper, M. S. 1973, ApJ, 181, 439
Dondoglio, E., Milone, A. P., Lagioia, E. P., et al. 2021, ApJ, 906, 76
Dutta, S. I., Ratković, S., & Prakash, M. 2004, PhRvD, 69, 023005
Dzhioev, A. A., Yudin, A. V., Dunina-Barkovskaya, N. V., & Vdovin, A. I. 2023, arXiv:2306.16055
Edvardsson, B., Andersen, J., Gustafsson, B., et al. 1993, A&A, 275, 101
El Eid, M. F., Meyer, B. S., & The, L.-S. 2004, ApJ, 611, 452
Farag, E., Renzo, M., Farmer, R., Chidester, M. T., & Timmes, F. X. 2022, ApJ, 937, 112
Farag, E., Timmes, F. X., Taylor, M., Patton, K. M., & Farmer, R. 2020, ApJ, 893, 133
Farmer, R., Fields, C. E., Petermann, I., et al. 2016, ApJS, 227, 22
Farmer, R., Fields, C. E., & Timmes, F. X. 2015, ApJ, 807, 184
Ferguson, J. W., Alexander, D. R., Allard, F., et al. 2005, ApJ, 623, 585
Ferguson, J. W., & Dotter, A. 2008, in IAU Symp. 252, The Art of Modeling Stars in the 21st Century, ed. L. Deng & K. L. Chan (Cambridge: Cambridge Univ. Press), 1
Fields, C. E., & Couch, S. M. 2021, ApJ, 921, 28
Fowler, W. A., & Hoyle, F. 1964, ApJS, 9, 201
Franz, N., Dennis, M., & Sakstein, J. 2023, arXiv:2307.13050
Fuller, G. M., Fowler, W. A., & Newman, M. J. 1985, ApJ, 293, 1

Gallino, R., Arlandini, C., Busso, M., et al. 1998, ApJ, 497, 388
García-Berro, E., Ritossa, C., & Iben, I., Jr. 1997, ApJ, 485, 765
Gautschy, A. 2012, arXiv:1208.3870
Gautschy, A. 2013, arXiv:1303.6652
Georgy, C., Ekström, S., Eggenberger, P., et al. 2013, A&A, 558, A103
Giannone, P., & Weigert, A. 1967, ZAp, 67, 41
Girardi, L. 1999, MNRAS, 308, 818
Glebbeek, E., Gaburov, E., de Mink, S. E., Pols, O. R., & Portegies Zwart, S. F. 2009, A&A, 497, 255
Graboske, H. C., Dewitt, H. E., Grossman, A. S., & Cooper, M. S. 1973, ApJ, 181, 457
Groh, J. H., Ekström, S., Georgy, C., et al. 2019, A&A, 627, A24
Hajduk, M., Todt, H., Hamann, W.-R., et al. 2020, MNRAS, 498, 1205
Hansen, C. J., Kawaler, S. D., & Trimble, V. 2004, Stellar Interiors: Physical Principles, Structure, and Evolution (New York: Springer-Verlag)
Harada, M., Abe, K., Bronner, C., et al. 2023, ApJL, 951, L27
Hartmann, D. H., & Woosley, S. E. 1997, APh, 7, 137
Hawkins, K., Leistedt, B., Bovy, J., & Hogg, D. W. 2017, MNRAS, 471, 722
Hayashi, C., Hōshi, R., & Sugimoto, D. 1962, PThPS, 22, 1
Heger, A., Fryer, C. L., Woosley, S. E., Langer, N., & Hartmann, D. H. 2003, ApJ, 591, 288
Heger, A., Woosley, S. E., Martínez-Pinedo, G., & Langanke, K. 2001, ApJ, 560, 307
Herwig, F. 2000, A&A, 360, 952
Herwig, F. 2002, Ap&SS, 279, 103
Herwig, F. 2005, ARA&A, 43, 435
Hirata, K., Kajita, T., Koshiba, M., Nakahata, M., & Oyama, Y. 1987, PhRvL, 58, 1490
Hirata, K. S., Kajita, T., Koshiba, M., et al. 1988, PhRvD, 38, 448
Hofmeister, E., Kippenhahn, R., & Weigert, A. 1964, ZAp, 60, 57
Horiuchi, S., Beacom, J. F., & Dwek, E. 2009, PhRvD, 79, 083013
Humphreys, R. M., & Davidson, K. 1979, ApJ, 232, 409
Hunter, J. D. 2007, CSE, 9, 90
Iben, I. J. 1963, ApJ, 138, 452
Iben, I. J., Kaler, J. B., Truran, J. W., & Renzini, A. 1983, ApJ, 264, 605
Iben, I. J., & Rood, R. T. 1970, ApJ, 159, 605
IceCube Collaboration 2023, Sci, 380, 1338
Iglesias, C. A., & Rogers, F. J. 1993, ApJ, 412, 752
Iglesias, C. A., & Rogers, F. J. 1996, ApJ, 464, 943
Irwin, A. W. 2004, The FreeEOS Code for Calculating the Equation of State for Stellar Interiors v2.2.1, http://freeeos.sourceforge.net/
Itoh, N., Adachi, T., Nakagawa, M., Kohyama, Y., & Munakata, H. 1989, ApJ, 339, 354
Itoh, N., Hayashi, H., Nishikawa, A., & Kohyama, Y. 1996a, ApJS, 102, 411
Itoh, N., Mutoh, H., Hikita, A., & Kohyama, Y. 1992, ApJ, 395, 622
Itoh, N., Nishikawa, A., & Kohyama, Y. 1996b, ApJ, 470, 1015
Itoh, N., Totsuji, H., Ichimaru, S., & Dewitt, H. E. 1979, ApJ, 234, 1079
Izzard, R. G., Lugaro, M., Karakas, A. I., Iliadis, C., & van Raai, M. 2007, A&A, 466, 641
Jermyn, A. S., Bauer, E. B., Schwab, J., et al. 2023, ApJS, 265, 15
Jermyn, A. S., Schwab, J., Bauer, E., Timmes, F. X., & Potekhin, A. Y. 2021, ApJ, 913, 72
José, J., Coc, A., & Hernanz, M. 1999, ApJ, 520, 347
Kantor, E. M., & Gusakov, M. E. 2007, MNRAS, 381, 1702
Kappeler, F., Beer, H., & Wisshak, K. 1989, RPPh, 52, 945
Käppeler, F., Gallino, R., Bisterzo, S., & Aoki, W. 2011, RvMP, 83, 157
Kato, C., Delfan Azari, M., Yamada, S., et al. 2015, ApJ, 808, 168
Kato, C., Hirai, R., & Nagakura, H. 2020a, MNRAS, 496, 3961
Kato, C., Ishidoshiro, K., & Yoshida, T. 2020b, ARNPS, 70, 121
Kato, C., Nagakura, H., Furusawa, S., et al. 2017, ApJ, 848, 48
Kemp, A. J., Karakas, A. I., Casey, A. R., Kobayashi, C., & Izzard, R. G. 2022, MNRAS, 509, 1175
Kosmas, T. S., Tsoulos, I., Kosmas, O., & Giannaka, P. G. 2022, FrASS, 8, 763276
Krauss, L. M., Glashow, S. L., & Schramm, D. N. 1984, Natur, 310, 191
Kroupa, P. 2001, MNRAS, 322, 231
Kutschera, M., Odrzywołek, A., & Misiaszek, M. 2009, AcPPB, 40, 3063
Kutter, G. S., & Savedoff, M. P. 1969, ApJ, 156, 1021
Kyutoku, K., & Kashiyama, K. 2018, PhRvD, 97, 103001
Lamb, S. A., Iben, I., Jr., & Howard, W. M. 1976, ApJ, 207, 209
Langanke, K., & Martínez-Pinedo, G. 2000, NuPhA, 673, 481
Lawlor, T. M. 2023, MNRAS, 519, 5373
Lecoanet, D., Schwab, J., Quataert, E., et al. 2016, ApJ, 832, 71
Lee, M. G., Freedman, W. L., & Madore, B. F. 1993, ApJ, 417, 553
Lejeune, T., Cuisinier, F., & Buser, R. 1998, A&AS, 130, 65
Leung, S.-C., Blinnikov, S., Ishidoshiro, K., Kozlov, A., & Nomoto, K. 2020, ApJ, 889, 75
Limongi, M., & Chieffi, A. 2018, ApJS, 237, 13
Lin, Z., & Lunardini, C. 2020, PhRvD, 101, 023016
Lunardini, C., & Winter, W. 2017, PhRvD, 95, 123001
Madore, B. F., Freedman, W. L., Owens, K. A., & Jang, I. S. 2023, AJ, 166, 2
Marion, J. B., & Fowler, W. A. 1957, ApJ, 125, 221
Meakin, C. A., & Arnett, D. 2007, ApJ, 667, 448
Mehta, A. K., Buonanno, A., Gair, J., et al. 2022, ApJ, 924, 39
Miller Bertolami, M. M., & Althaus, L. G. 2007, MNRAS, 380, 763
Misiaszek, M., Odrzywołek, A., & Kutschera, M. 2006, PhRvD, 74, 043006
Mitalas, R. 1985, ApJ, 290, 273
Monpribat, E., Martinet, S., Courtin, S., et al. 2022, A&A, 660, A47
Mukhopadhyay, M., Lunardini, C., Timmes, F. X., & Zuber, K. 2020, ApJ, 899, 153
Müller, B., Melson, T., Heger, A., & Janka, H.-T. 2017, MNRAS, 472, 491
Murai, T., Sugimoto, D., Hōshi, R., & Hayashi, C. 1968, PThPh, 39, 619
Nabi, J.-U., Ullah, A., & Khan, A. A. 2021, ApJ, 911, 93
Naumov, V. A. 2011, PPNL, 8, 683
Nieuwenhuijzen, H., & de Jager, C. 1990, A&A, 231, 134
Nomoto, K., & Hashimoto, M. 1988, PhR, 163, 13
Nugis, T., & Lamers, H. J. G. L. M. 2000, A&A, 360, 227
Oda, T., Hino, M., Muto, K., Takahara, M., & Sato, K. 1994, ADNDT, 56, 231
Odrzywołek, A. 2007, EPJC, 52, 425
Odrzywolek, A. 2009, PhRvC, 80, 045801
Odrzywolek, A., & Heger, A. 2010, AcPPB, 41, 1611
Odrzywolek, A., Misiaszek, M., & Kutschera, M. 2004, APh, 21, 303
OpenAI 2023, arXiv:2303.08774
Patton, K. M., Lunardini, C., & Farmer, R. J. 2017a, ApJ, 840, 2
Patton, K. M., Lunardini, C., Farmer, R. J., & Timmes, F. X. 2017b, ApJ, 851, 6
Paxton, B., Bildsten, L., Dotter, A., et al. 2011, ApJS, 192, 3
Paxton, B., Cantiello, M., Arras, P., et al. 2013, ApJS, 208, 4
Paxton, B., Marchant, P., Schwab, J., et al. 2015, ApJS, 220, 15
Paxton, B., Schwab, J., Bauer, E. B., et al. 2018, ApJS, 234, 34
Paxton, B., Smolec, R., Schwab, J., et al. 2019, ApJS, 243, 10
Peña, M., Parthasarathy, M., Ruiz-Escobedo, F., & Manick, R. 2022, MNRAS, 515, 1459
Peters, J. G. 1968, ApJ, 154, 225
Piersanti, L., Bravo, E., Straniero, O., Cristallo, S., & Domínguez, I. 2022, ApJ, 926, 103
Pignatari, M., Gallino, R., Heil, M., et al. 2010, ApJ, 710, 1557
Pignatari, M., Hirschi, R., Wiescher, M., et al. 2013, ApJ, 762, 31
Piro, A. L., Giacomazzo, B., & Perna, R. 2017, ApJL, 844, L19
Planck Collaboration, Ade, P. A. R., Aghanim, N., et al. 2016, A&A, 594, A13
Porciani, C., Petroni, S., & Fiorentini, G. 2004, APh, 20, 683
Potekhin, A. Y., & Chabrier, G. 2010, CoPP, 50, 82
Poutanen, J. 2017, ApJ, 835, 119
Prantzos, N., Hashimoto, M., & Nomoto, K. 1990, A&A, 234, 211
Prša, A., Harmanec, P., Torres, G., et al. 2016, AJ, 152, 41
Raiteri, C. M., Busso, M., Gallino, R., & Picchio, G. 1991a, ApJ, 371, 665
Raiteri, C. M., Busso, M., Gallino, R., Picchio, G., & Pulone, L. 1991b, ApJ, 367, 228
Ratcliffe, B., Minchev, I., Anders, F., et al. 2023, MNRAS, 525, 2208
Ratković, S., Iyer Dutta, S., & Prakash, M. 2003, PhRvD, 67, 123002
Reimers, D. 1977, A&A, 61, 217
Reindl, N., Rauch, T., Miller Bertolami, M. M., Todt, H., & Werner, K. 2017, MNRAS, 464, L51
Reusch, S., Stein, R., Kowalski, M., et al. 2022, PhRvL, 128, 221101
Ritter, C., Andrassy, R., Côté, B., et al. 2018, MNRAS, 474, L1
Rogers, F. J., & Nayfonov, A. 2002, ApJ, 576, 1064
Sabhahit, G. N., Vink, J. S., Higgins, E. R., & Sander, A. A. C. 2021, MNRAS, 506, 4473
Sallaska, A. L., Iliadis, C., Champange, A. E., et al. 2013, ApJS, 207, 18
Salpeter, E. E. 1955, PhRv, 97, 1237
Sandage, A. 1986, ARA&A, 24, 421
Sanyal, D., Langer, N., Szécsi, D., -C Yoon, S., & Grassitelli, L. 2017, A&A, 597, A71
Sarajedini, A. 1999, AJ, 118, 2321
Saumon, D., Chabrier, G., & van Horn, H. M. 1995, ApJS, 99, 713
Schwarzschild, M., & Härm, R. 1965, ApJ, 142, 855
Serenelli, A., & Weiss, A. 2005, A&A, 442, 1041
Serenelli, A., Weiss, A., Cassisi, S., Salaris, M., & Pietrinferni, A. 2017, A&A, 606, A33
Serenelli, A. M., & Fukugita, M. 2005, ApJL, 632, L33
Siess, L. 2007, A&A, 476, 893
Siess, L. 2010, A&A, 512, A10
Simpson, C., Abe, K., Bronner, C., et al. 2019, ApJ, 885, 133

Stonehill, L. C., Formaggio, J. A., & Robertson, R. G. 2004, PhRvC, 69, 015801
Sukhbold, T., & Adams, S. 2020, MNRAS, 492, 2578
Sukhbold, T., Ertl, T., Woosley, S. E., Brown, J. M., & Janka, H. T. 2016, ApJ, 821, 38
Sukhbold, T., & Woosley, S. E. 2014, ApJ, 783, 10
Sukhbold, T., Woosley, S. E., & Heger, A. 2018, ApJ, 860, 93
Suliga, A. M. 2022, arXiv:2207.09632
Takahashi, K., Takiwaki, T., & Yoshida, T. 2023, ApJ, 945, 19
Tan, W. P., Boeltzig, A., Dulal, C., et al. 2020, PhRvL, 124, 192702
The, L.-S., El Eid, M. F., & Meyer, B. S. 2007, ApJ, 655, 1058
Thomas, H.-C. 1967, ZAp, 67, 420
Timmes, F. X., Brown, E. F., & Truran, J. W. 2003, ApJL, 590, L83
Timmes, F. X., & Swesty, F. D. 2000, ApJS, 126, 501
Timmes, F. X., Townsend, R. H. D., Bauer, E. B., et al. 2018, ApJ, 867, L30
Timmes, F. X., Woosley, S. E., & Taam, R. E. 1994, ApJ, 420, 348
Timmes, F. X., Woosley, S. E., & Weaver, T. A. 1996, ApJ, 457, 834
Tompkins, S., Windhorst, R., Young, P., & Timmes, F. X. 2020, RNAAS, 4, 172
Townsend, R. H. D. 2019a, MESA SDK for Linux, v20190503, Zenodo, doi:10.5281/zenodo.2669541
Townsend, R. H. D. 2019b, MESA SDK for Mac OS, v20190503, Zenodo, doi:10.5281/zenodo.2669543
Townsley, D. M., Jackson, A. P., Calder, A. C., et al. 2009, ApJ, 701, 1582
van der Walt, S., Colbert, S. C., & Varoquaux, G. 2011, CSE, 13, 22
van Horn, H. M. 1971, in IAU Symp. 42, White Dwarfs, ed. W. J. Luyten (Dordrecht: Springer), 97
Vandenberg, D. A. 1983, ApJS, 51, 29
VandenBerg, D. A., Casagrande, L., & Edvardsson, B. 2022, MNRAS, 509, 4208
Vartanyan, D., Burrows, A., Radice, D., Skinner, M. A., & Dolence, J. 2018, MNRAS, 477, 3091
Vila, S. C. 1966, ApJ, 146, 437
Vink, J. S., de Koter, A., & Lamers, H. J. G. L. M. 2001, A&A, 369, 574
Vishniac, E. T. 2023, BAAS, 55, 016
Vogel, P., & Beacom, J. F. 1999, PhRvD, 60, 053003
Wang, S., & Chen, X. 2021, ApJ, 923, 145
Weaver, T. A., & Woosley, S. E. 1993, PhR, 227, 65
Weiss, A., Cassisi, S., Schlattl, H., & Salaris, M. 2000, ApJ, 533, 413
Wiescher, M., deBoer, R. J., & Görres, J. 2023, EPJA, 59, 11
Wiescher, M., Gorres, J., Graff, S., Buchmann, L., & Thielemann, F. K. 1989, ApJ, 343, 352
Wiescher, M., Görres, J., Uberseder, E., Imbriani, G., & Pignatari, M. 2010, ARNPS, 60, 381
Winter, W., & Lunardini, C. 2023, ApJ, 948, 42
Woosley, S. E., & Heger, A. 2015, ApJ, 810, 34
Woosley, S. E., Heger, A., & Weaver, T. A. 2002, RvMP, 74, 1015
Woosley, S. E., & Weaver, T. A. 1986, ARA&A, 24, 205
Xu, H. Y., & Li, Y. 2004, A&A, 418, 213
Yang, Y. & JUNO Collaboration 2022, NIMPA, 1042, 167435
Young, P. A. 2018, in Handbook of Exoplanets, ed. H. J. Deeg & J. A. Belmonte (Cham: Springer), 2959
Yusof, N., Abu Kassim, H., Garba, L. G., & Ahmad, N. S. 2021, MNRAS, 503, 5965
Zhang, W., Woosley, S. E., & Heger, A. 2008, ApJ, 679, 639
Zhao, L., Song, H., Meynet, G., et al. 2023, A&A, 674, A92
Zickefoose, J., Di Leva, A., Strieder, F., et al. 2018, PhRvC, 97, 065806